Characterization and calibration of a liquid xenon time projection chamber

Masterarbeit

vorgelegt der Mathematisch-naturwissenschaftlichen Fakultät
der
Universität Zürich

von
Hrvoje Dujmović

Betreuung

Prof. Dr. Laura Baudis
Dr. Alexander Kish

Zürich 2014

Contents

Astronomical observations indicate that the Standard Model particles compose only about 17% of the matter content in the Universe. The remaining matter is referred to as "dark matter", and its nature is one of the biggest open questions in modern physics. The motivation for the dark matter and the methodology of the dark matter search is presented in the first chapter. Liquid xenon detectors are very suitable for direct dark matter searches. One such experiment is XENON, located in Laboratori Nazionali del Gran Sasso, Italy. As a part of the XENON collaboration, the group in Zürich has been working on small liquid xenon chambers, Xurich I and its successor Xurich II. Xurich I measured the response of liquid xenon to low-energy gammas. Xurich II on the other hand is designed to measure the response to low-energy neutrons for different recoil energies. The small size of the chambers simplifies the measurements of these properties, and the results obtained from it are vital for the proper interpretation of the data from larger xenon detectors.

The second chapter of this thesis will focus on various simulations and software development for the Xurich II detector. The final chapter focuses on various laboratory tests that were performed for the buildup of the detector.

Chapter 1

Introduction

1.1 Dark matter evidence

What makes the search for dark matter a particularly interesting field of research is the overwhelming amount of evidence for its existence. Different astronomical observations on various scales all indicate that the Standard Model particles can not possibly account for all the matter in the Universe. The scales range from the comparably small galactic scale to the entire observable Universe. A selection of these observations is presented here as motivation for the search for dark matter.

1.1.1 Rotation curves of galaxies

A spiral galaxy is characterized by its flat rotating disc that surrounds the central stellar bulge. If one looks at a spiral galaxy which is edge-on from our point of view, one expects the spectral lines to be red- or blue-shifted due to the rotation of the galaxy. This effect can be observed at many different wavelengths, from radio waves to x-rays. One of the most interesting ones is the 21 cm line emitted by neutral hydrogen [1]. This allows for the probing of the vast gas clouds that extend further out than the stars in a galaxy.

Looking at the redshift of these lines as a function of the distance from the galactic center allows us to create a so-called rotation curve of the galaxy, telling us how fast the galaxy is rotating at which point. Simple Newtonian mechanics gives us the relation between the rotation curve and the mass distribution in the galaxy:

$$r\, v(r)^2 = G\, M(r),$$

where $v(r)$ denotes the rotation velocity at the distance r from the galactic center, and $M(r)$ the mass comprised inside the radius. The density of the stars and the interstellar gas in a galaxy drops off rapidly at large radii. From this one would expect the rotational velocity to start dropping off with radius as well. One finds however that every measured rotation curve for spiral galaxies becomes more or less flat at large radii. An example of such a rotation curve compared to the expectation is shown in 1.1.1.

One of the simplest solutions for the apparent discrepancy is postulation of a dark matter halo around the galaxy. The halo isn't directly observable since dark matter does not emit or reflect light, but the mass of the halo accounts for the excess in the observed rotation curve.

1.1.2 Velocity dispersion in galaxies

In contrast to a spiral galaxy with its clear structure, an elliptical galaxy shows no apparent structure, and its stars are in seemingly random orbits around the center. Thus the concept of the rotation curves does not make much sense in the context of elliptical galaxies. However one can still take a statistical approach to come to a similar conclusion as the one for the spiral galaxies.

If one looks at the spectrum of such an elliptical galaxy, an abnormal broadening of the spectral lines [3] can be observed. Similarly to the observations made with the spiral galaxies, the 21 cm neutral hydrogen line is especially useful for this, since it encompasses a much bigger area than observations made

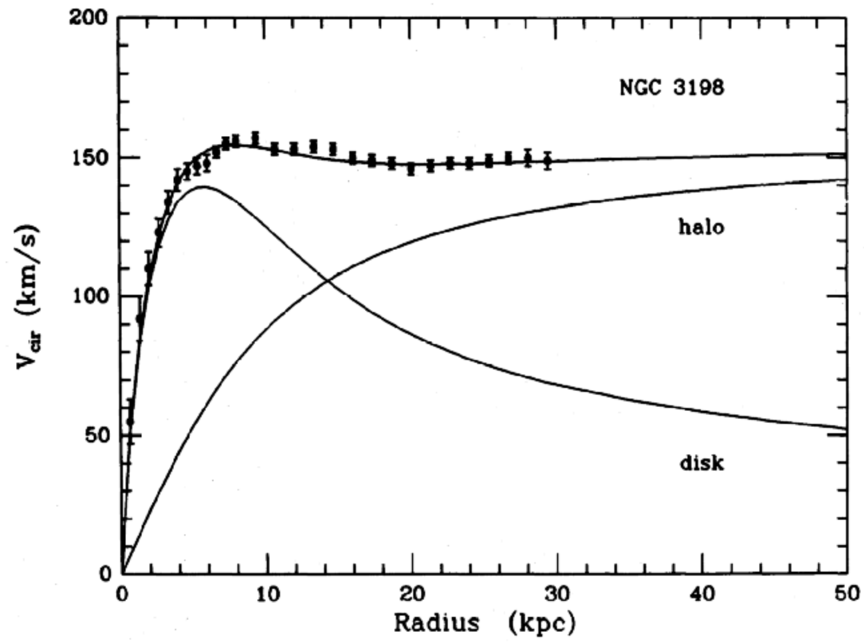

Figure 1.1.1: The rotation curve of the NGC 3198 galaxy [2]. The data points represent the measured rotation velocity for objects at certain distances from the galactic center. The disk curve shows the expected curve if the galaxy was only made up of visible matter. The halo curve shows the expected dark matter contribution. The sum of the two is fitted to the data points.

in the visible spectrum. The broadening is due to the random direction of motion of the stars. From the width of the lines one can calculate the average velocity of the stars in the galaxy.

Statistical mechanics provides us with the so-called virial theorem which relates the time-averaged kinetic and potential energies of a system:

$$\langle V \rangle = -2 \langle T \rangle$$

From the velocity of the stars one can calculate the right part of the equation. The left part of the equation directly relates to the total mass inside the galaxy. If we compare this virial mass of the galaxy to the mass of the observable stars and gas clouds, once again we find a major discrepancy [4]. An evident explanation for this discrepancy is the existence of some sort of invisible mass - the dark matter.

1.1.3 Velocity dispersion in galaxy clusters

The virial method described in the previous section can be extended to galaxy clusters. The redshift of the spectra of the individual galaxies in a cluster can be used to calculate the velocity of the galaxy. If one sums up the kinetic energy of all the galaxies and relates it to the total potential energy due to the visible mass of the cluster, this would once again result in a large discrepancy.

This method was notably used by Fritz Zwicky [5] and was historically the first hint for the existence of the dark matter.

1.1.4 Gravitational lensing

A more modern method of measuring the mass distribution in a galaxy cluster is the use of the gravitational lensing. Gravitational lensing relies on the fact that massive objects bend light rays moving close to it. If one tries to look at a distant object with a galaxy cluster close to the line of sight, the observed image is distorted due to cluster gravitationally bending the light. From the observed distortion information about mass distribution in the cluster can be obtained [6].

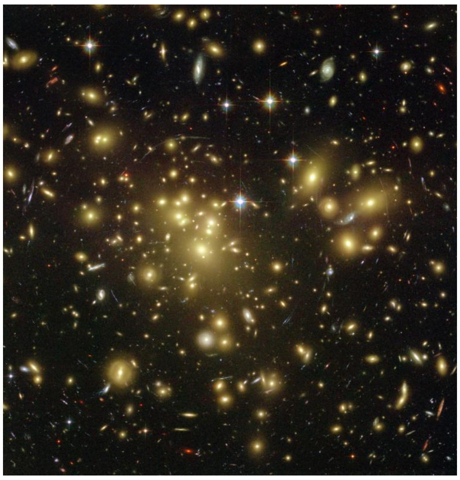

Figure 1.1.2: An example of gravitational lensing in the Abell 1689 cluster. The mass of the cluster distorts the images of the galaxies seen behind it [7].

One of the most convincing arguments for the existence of dark matter uses the method of gravitational lensing to measure the mass distribution inside in galaxy cluster. The Bullet cluster is an example of such a cluster [8]. It actually consists of two colliding galaxy clusters. Gravitational lensing studies provide us with the mass distribution in the cluster. Direct observations of the galaxies in the cluster and the observations of the x-ray emitting intergalactic plasma give us the distribution of the baryonic matter in the cluster. Interestingly, there seems to be a significant spatial offset between the two mass distributions which can be seen in figure 1.1.3. Dark matter could beautifully explain this discrepancy; when the two clusters collided, the non-interacting dark matter halos of the clusters passed right through each other, while the baryonic matter gets dragged behind due to the electromagnetic interactions with the other cluster.

What makes the gravitational lensing such a great argument for the existence of dark matter is the fact that most the other examples discussed here could possibly be explained by modifying the laws of gravity. However, most of these models of modified gravity fail to explain the behavior of the Bullet cluster, since it is extremely difficult to come up with a consistent theory of gravity that would predict an offset between the center of mass and the center of gravity.

1.1.5 Cosmic microwave background radiation

Roughly 380'000 years after the Big Bang the Universe cooled down enough to form neutral atoms. This process made the Universe transparent, and the photons from that time form what is known as the cosmic microwave background (CMB) radiation. The CMB can be observed today as a smooth isotropic $T = 2.7\,\mathrm{K}$ black body radiation [10]. Precise measurements of the CMB show that it is not perfectly uniform, but is a subject to small fluctuations on the μK scale. From these fluctuations one can gather a lot of information about the composition of the Universe at the time of the thermal decoupling. Amongst other things one can determine the relative abundance of gravitationally interacting matter in the Universe and the abundance of electromagnetically interacting matter. The measured values for the baryonic and the total matter components are [11]:

$$\Omega_b = 0.0456(16), \qquad \Omega_m = 0.2726(17).$$

The large discrepancy between the two is definitely a strong indication for the existence of dark matter.

1.2 Dark matter candidates

In the previous section we have established the existence of dark matter. A brief discussion of particles that could potentially explain the dark matter phenomena can be found in this section. For more detailed

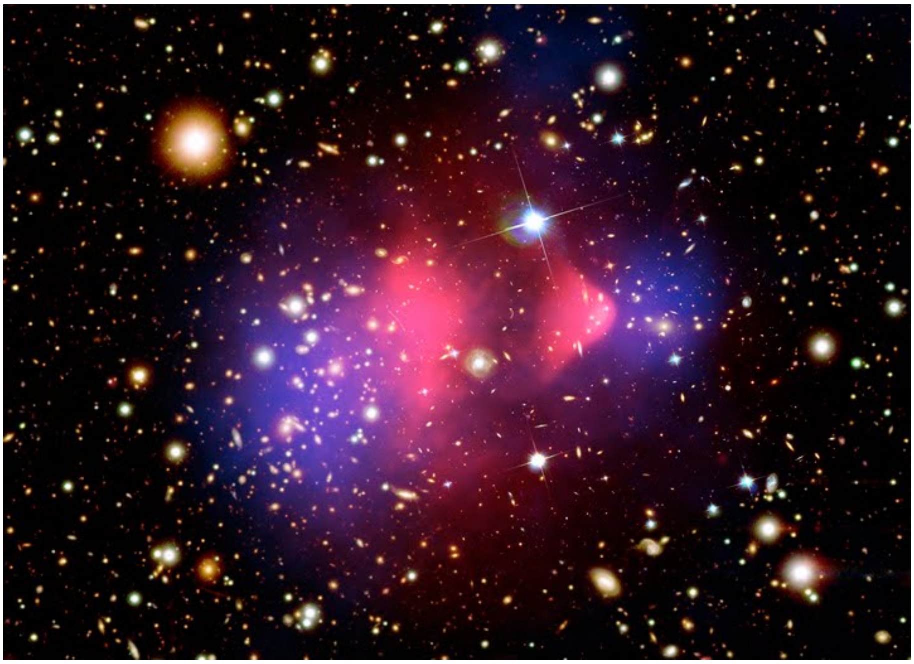

Figure 1.1.3: An image of the Bullet Cluster. In yellow are galaxies as seen from the visible spectrum. Red color represents the intergalactic gas clouds measured in the x-ray spectrum. In blue is the mass distribution as calculated from the lensing data. One can clearly see the discrepancy between the center of mass and the center of baryonic mass [9].

discussion see [13].

1.2.1 Standard Model candidates

The astronomical observations give us the requirements that a potential dark matter particle has to be non-baryonic, stable and electromagnetically non-interacting. The Standard Model indeed has a particle with these properties, namely the neutrino. The neutrinos were considered a dark matter candidate, however the precision measurements of the CMB have placed a very strong limit on the total neutrino density in the Universe [14]. This limit is far too low to account for any significant contribution of the neutrinos to the total dark matter density in the Universe. This excludes the possibility of explaining the dark matter without the introduction of a new particle.

1.2.2 Beyond the Standard Model

Theoretical physics provides us with a large number of different extensions to the Standard Model [13]. Most of these theories introduce a new particle that could explain the dark matter phenomenon. The detailed properties of these particles are highly model-dependent, and a detailed discussion would go far beyond the scope of this work.

Some general model-independent considerations can be made about the particles. The only requirement is that some time after the Big Bang the particle was in a thermal equilibrium with the rest of the Universe [15]. As the Universe expands it cools down, and at some point the temperature drops below the mass of the particle. At that point the production of the particle stops, and the so-called relic density of the particle remains. The density depends on the reaction cross section and the average velocity of the particle. Due to structural constrains from the CMB measurements one can set a lower limit on the mass of the dark matter particle at roughly 10 keV. Due to the mass constrain and the fact that the particle can not be interacting strongly with the baryonic matter, the particle type is generally labeled as the Weakly Interacting Massive Particle (WIMP) [16].

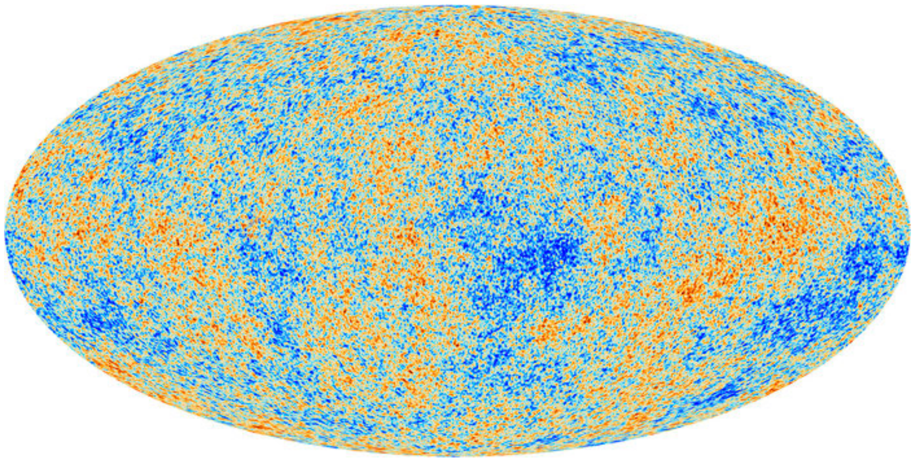

Figure 1.1.4: The all-sky map taken with the Planck satellite. The temperature of the radiation is color coded. The fluctuations give us a lot of information about the composition of the Universe, showing the discrepancy between the amount of baryonic and total matter in the Universe [12].

1.3 Direct dark matter detection

In the previous chapters we have introduced a class of potential dark matter candidates, WIMPs. This chapter will go into more detail about the methods used in the attempt to directly detect WIMPs in our surrounding.

1.3.1 Dark matter interactions

From the observations of spiral galaxies and from gravitational simulations of the development of a galaxy one can obtain a rough idea about how the dark matter halo looks like, and create different models with different halo profiles. Using the information we have about the velocities of the Sun and other stars in the solar neighborhood around the galactic center, we can attempt to fit such a halo profile to the Milky Way. This gives us an estimate about the velocity distribution and the local density of dark matter. The exact numbers are highly model-dependent, but most estimates are around $\rho_\chi = 0.4\,\mathrm{GeV/cm^3}$ for the density and $\sigma_v = 300\,\mathrm{km/s}$ for the velocity dispersion [17].

The mass of WIMPs that is the most interesting from a theoretical point of view is in the GeV-TeV scale [6]. At these masses one does not expect WIMPs to interact with the electrons in a material, but rather with the nucleus. From simple considerations one comes with the formula for the interaction rate per unit mass per unit time:

$$R = \rho_\chi v \, \frac{1}{m_n} \, \frac{\sigma}{m_\chi} \, ,$$

where the first two terms describe the local dark matter density and velocity and are obtained from the galactic halo models described earlier. The third term is the mass of the target nucleus and is related to the detector material. The last term is the cross section and the mass of the WIMP. Since we have not yet found WIMP, the values of these two parameters are unknown.

The most important type of interaction to consider between a WIMP and a nucleus is the elastic spin-independent scattering. With some approximations it turns out that the cross section for this type of interaction scales with the second power of the mass of the nucleus [15].

1.3.2 Direct detection principles

Because of the very low interaction cross section, in order to detect WIMPs one wants to maximize the potential interaction rate while minimizing the background rate [18]. This places some constraints on detector materials that can be used; heavy elements are favored because they offer a larger interaction cross section. Low natural radioactivity is very important in order to minimize the intrinsic background.

Liquid xenon fulfills most of these requirements rather well and is an excellent candidate for the use as detector material. The scalability of a detector is much simpler for a liquid detector then for solid crystal such as e.g. germanium. Furthermore, liquid xenon allows to use robust methods of distinguishing between nuclear recoil events and the, mainly electromagnetic, background from the cosmic rays and radioactivity in the surrounding materials. Several steps are taken in order to minimize the impact of the said background on the measurements. Placing the detector into an underground facility allows for very good shielding against cosmic rays. The use of a big detector volume not only increases the number of expected events for a given interaction rate, but also allows the application of self-shielding to reduce the background. Because of the high Z xenon has a radiation length of only a couple of centimeters, thus most gamma rays will interact in the outer parts of the detector. If one cuts out the events at the edge of the detector and only considers the inner volume, it is possible to strongly suppress the background. This procedure is possible because xenon detectors have good position reconstruction.

Particles interacting in liquid xenon deposit their energy in three different ways; scintillation light, ionisation and phonons (heat). The detection of phonons is difficult and requires very low temperatures, thus liquid xenon detectors focus on the detection of the scintillation and ionisation signals. The ratio of the energy deposited in each of the three channels depends on the total deposited energy, the type of interaction and various external factors. Understanding of these relations is vital for the event reconstruction in any liquid xenon detector. The study of these relations is the main focus of the Xurich II project and this thesis.

1.4 Liquid xenon time-projection chambers

The most common type of liquid xenon dark matter detectors uses a dual-phase time-projection chamber (TPC) in order to measure the scintillation and ionisation signals. The working principles of such a chamber will be discussed mainly using the example of the XENON100 TPC [20]. The same concepts apply to other xenon TPCs like LUX [21], XENON1T [22], the successor of XENON100 and to some extent Xurich I and Xurich II which will be discussed in the next chapter.

1.4.1 The XENON project

The XENON experiment is one of the most sensitive direct dark matter search experiments in the world. Since the expected WIMP interaction rate is very low (at most a couple of events per year per ton of detector material), it is extremely important to reduce the background as much as possible. This is why the experiment is located in Laboratori Nazionali de Gran Sasso, an underground laboratory in Italy, where the 1400 m of rock above the experiment act as an excellent shielding from the cosmic rays. The overlaying rock layer is 1400 m thick, corresponding to a shielding of 3600 m.w.e. and resulting in a background reduction by a factor of 10^6 [19].

XENON100 is a TPC: the main xenon volume is in the liquid phase and this is where most of the interactions happen. The interaction with a xenon atom generates scintillation, free electrons and phonons. This type of detector focuses on the detection of the first two channels, and from that one can try to extrapolate the total deposited energy. Two arrays of photomultiplier tubes (PMTs) are located at the top and bottom of the chamber. These PMTs make the detection of the direct scintillation light (S1) relatively simple. In order to detect the ionisation signal, a strong electric field is created across the chamber with the help of three electrodes, the cathode, the gate and the anode. Due to this field the electrons drift from the interaction point upwards. Once they reach the liquid surface they get extracted and enter the gas phase. The electric field in the gas phase is even higher and thus the electrons produce an avalanche, resulting in secondary scintillation (S2) proportional to the ionisation signal. This secondary scintillation can be detected by the PMT arrays resulting in the typical signals with one prompt and short S1 peak and a delayed broadened S2 peak. A schematic of a typical xenon TPC can be seen in 1.4.1.

In order to properly interpret the measurements done with dual-phase xenon TPCs one needs to be able to relate the scintillation and ionisation signals to the total energy deposited in the interaction. This conversion depends on the type of interaction. If a particle interacts with an electron in a xenon atom one speaks of electronic recoils, if the particle interacts with the xenon nucleus one speaks of nuclear recoils. For electronic recoils the conversion is determined by calibrating the detector with a gamma source of a

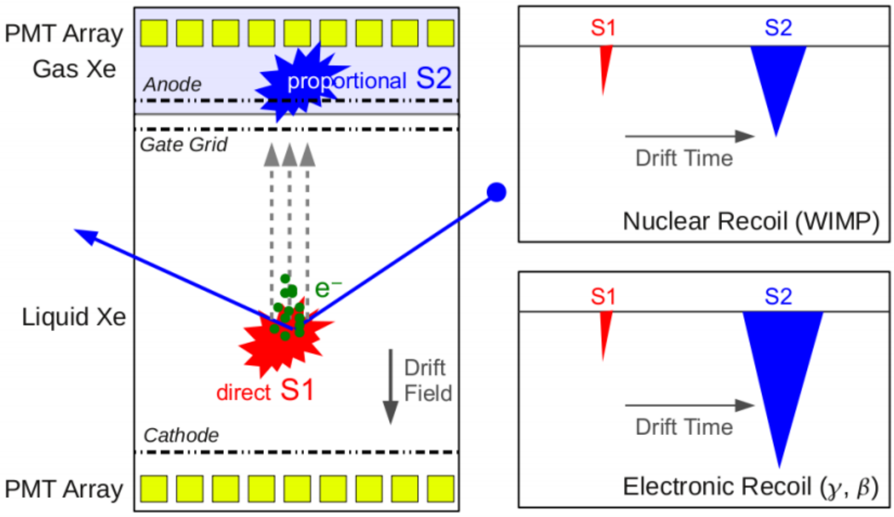

Figure 1.4.1: Particle detecton principle with a dual-phase xenon TPC [20].

known energy. For nuclear recoils it is done indecently by rescaling the scale for electromagnetic recoils. The conversion factor, $\mathcal{L}_{eff}$, has an energy dependence. The uncertainty on $\mathcal{L}_{eff}$ directly translates to an uncertainty on the energy scale and is one of the main systematics in the XENON100 results.

Chapter 2

Measurements of relative scintillation efficiency for nuclear recoils

When looking at the deposited energy of an event one can calculate the ratio between the ionisation and the scintillation signals. When looking at electromagnetic recoils, this ratio is higher then for nuclear recoils. This trait is very useful when distinguishing between potential WIMP signals which are always nuclear interactions and the predominantly electromagnetic background.

When particles interact with a xenon atom, some portion of the deposited energy gets converted to phonons (heat) and it is not directly measurable. So in order to be able to properly reconstruct an event one needs a method to relate the measured deposited energy to the total deposited energy. For electromagnetic interactions a detector can be calibrated by using a radioactive gamma source with a known energy and measure the response. For nuclear recoils this procedure is more complicated and impossible to perform on a large detector, thus an indirect calibration method is applied. The relative scintillation efficiency for nuclear recoils, usually refereed to as $\mathcal{L}_{eff}$, is defined as the ratio of the deposited number of energy quanta (ionisation electrons and scintillation photons) for a nuclear recoil and an electromagnetic recoil of the same energy [23]. For historical reason the $\mathcal{L}_{eff}$ is normalizedto the scintilation yield at 122 keV (energy of ^{57}Co). Thus if the energy scale for electronic recoils is known from the calibration and the value of $\mathcal{L}_{eff}$ is known for the given energy, it is possible to reconstruct the energy scale for the nuclear recoils.

The behavior of $\mathcal{L}_{eff}$ with energy is studied both theoretically and experimentally [24, 25, 26]. Down to roughly 20 keV $\mathcal{L}_{eff}$ is known pretty well, however it is not very clear what happens at lower energies and different measurements yield somewhat conflicting results (figure 2.0.1).

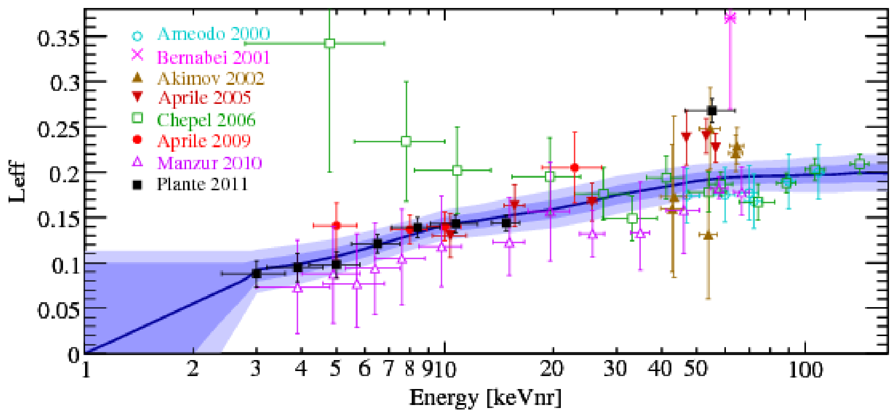

Figure 2.0.1: Different measurements of $\mathcal{L}_{eff}$. Below roughly 20 keV $\mathcal{L}_{eff}$ the results seem to partially disagree and the errors are pretty substantial [29].

2.1 Measurement principle

For nuclear recoil measurements one uses neutrons. Thus for the purpose of these measurements a specialized neutron generator is used. The generator uses a deuterium fusion process to create a monochromatic neutron beam. The Xurich II TPC is placed in the beam and two organic scintillators are positioned behind the TPC. The neutrons can scatter elastically off a xenon nucleus in the TPC. If they scatter under the right angle they can be detected by the organic scintillator. If one requires a coincidence between the events in the TPC and the scintillator, one can gain insight into the kinematics of the scattering. From this information and the initial neutron energy, an estimate of the energy deposited in the detector can be performed. For more precise values a detailed Monte Carlo simulation of the setup is required. For more details on the generator and the experimental setup are given in [27, 28]. For a sketch of the setup see figure 2.1.1.

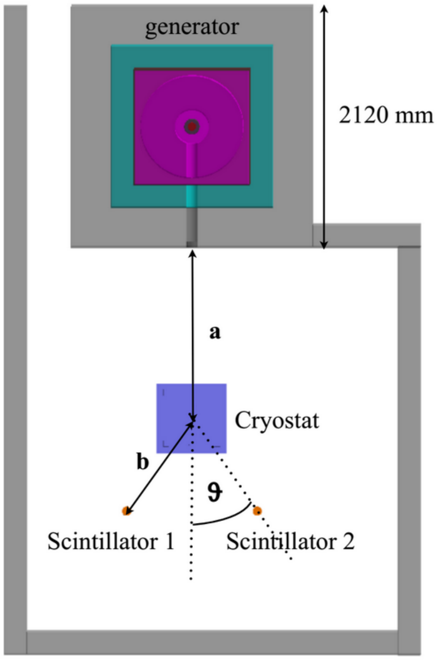

Figure 2.1.1: Setup of the neutron measurement. On top is the generator with the shielding. The TPC is in the cryostat in the middle. The two scintillators are behind it. Diagram from [27].

2.2 The Xurich II detector

Xurich I measured the response of xenon to electronic recoils down to 1.5 keV [30]. In contrast, the main goal of the Xurich II detector is to measure the response to nuclear recoils down to the energies of a couple keV.

2.2.1 Xurich II design

In figure 2.2.2 a schematic of the Xurich II TPC is shown. The active detector volume consists of a PTFE chamber filled with xenon. The cryostat is cooled down to roughly $170 - 180\,\mathrm{K}$, allowing to have the xenon in both liquid and gas phases. The cryostat and the gas systems are the same ones used for Xurich I. More details about them can be found in [33]. The TPC is surrounded by a 3 mm thivk PTFE reflector. Three grids made out of very thin Be-plated copper wires are placed in the chamber and are used as electrodes. The cathode grid is placed near the bottom of the chamber and is connected to a negative high voltage supply. The anode grid is placed slightly above (roughly 2 mm) the liquid level and is connected to a positive high voltage supply. The third grid is called the gate. It is grounded and placed below (roughly 2 mm) the liquid level. Above the anode and below the cathode there are two photomultiplier tubes (PMTs). The PMTs used for the experiment are Hamamatsu R9869, the same ones that were used in the previous version of Xurich. The cathode voltage can be set between roughly $1\,\mathrm{kV} - 9\,\mathrm{kV}$, resulting in drift fields of $0.2\,\mathrm{kV/cm} - 2.6\,\mathrm{kV/cm}$, resulting in total drift time of up to $20\,\mu\mathrm{s}$. The extraction efficiency of the electrons from the liquid surface depends on the field and reaches 100% at around $10\,\mathrm{kV/cm}$ [31]; for Xurich II geometry this corresponds to roughly $4\,\mathrm{kV}$ anode voltage. The extraction efficiency as a function of field can be seen in figure 2.2.1.

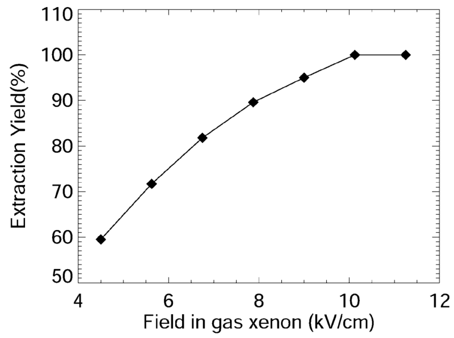

Figure 2.2.1
Electron extraction yield as a function of electric field in the gas phase. At a field higher than 10 kV/cm, all drifting electrons can be extracted from the liquid to the gas xenon [31].

As established in the previous chapter, once a particle scatters in the liquid xenon chamber it creates scintillation (photons) and ionisation (free electrons). The scintillation light is directly detected by the two PMTs and creates a very fast signal usually refereed to as S1. The free electrons form an electron cloud. If the interaction happened between the cathode and the gate, the cloud drifts upwards due to the strong electromagnetic field created by the electrodes. The field between the gate and the anode is even stronger and it allows the electrons that reach the liquid surface to be extracted into the gas phase. In the gas phase the electrons get accelerated rapidly and via an electroluminescence process they create secondary scintillation signal refereed to as S2. The S2 signals are typically much stronger, wider and have a longer delay compared to the almost instantaneous S1 signals. An example of the Xurich II trace can be seen in figure 2.2.3.

By studying the shape, the amplitude and the timing difference between the S1 and the S2 signals and comparing these vales between the two PMTs one can gather the information required for the reconstruction of the event.

In order to monitor the operation of the TPC and improve the quality of the signal, several systems are in place. A PT100 sensor is mounted on the bottom of the chamber and is used to monitor the temperature. Since impurities in the liquid xenon can have a strong negative impact on the signal quality, the chamber is connected to a gas system that constantly recirculates and purifies the xenon using a hot temperature zirconium getter. In order to ensure an optimal extraction of the electrons into the gaspahse, it is important for the liquid level to be in a specific position between the gate and the anode and also parallel to the grids. Three pairs of metallic plates are placed around the chamber and the capacitance between the plates is monitored. Since liquid and gas xenon have different dielectric constants, the capacitance depends on the liquid level between the plates. Thus from the capacitance it is possible to determine the liquid level and potentially do some adjustments to it when necessary. A forth, cylindrical, level meter is placed in the metallic weir on the side of the chamber. The weir is a part of the recirculation system and the level meter inside is mainly used to monitor the recirculation, and it facilitates the procedure of filling the chamber with xenon by monitoring the overall level in the chamber.

Since the scintillation and ionisation yields depend on the electric field at the point of interaction, in order to improve the accuracy of the measurement it is important for the field in the main interaction volume to be as uniform as possible. For this purpose a series of 7 field shaping rings is placed around the chamber. These rings and the electrodes are connected through a series of resistors that ensure the rings are at the right potential and the field is as uniform as possible. For more details on the design of the Xurich II field shaping system see [32]. Most of residual uniformities of the field are near the edges

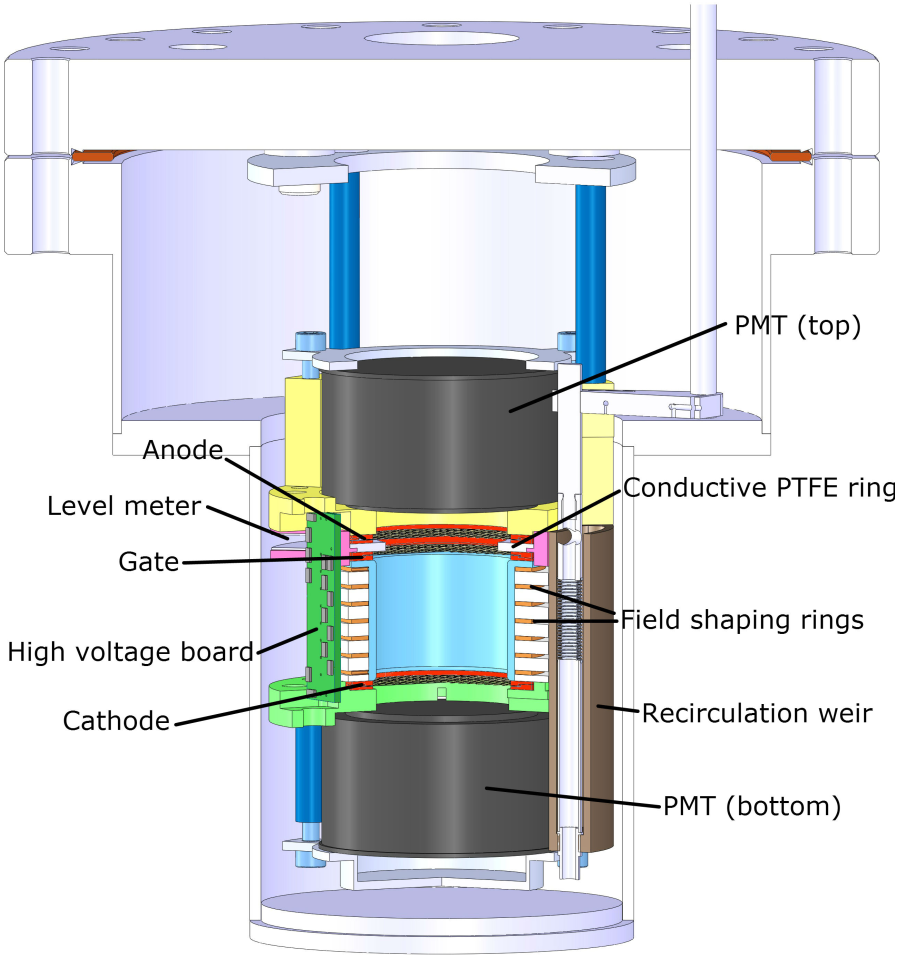

Figure 2.2.2: Xurich II schematic. The electrode grids are in red, the two PMTs in black. On the right hand side one can see the recirculation weir. On the left hand site in green is the high voltage board connecting to the field shaping rings and the electrodes.

of the chamber. There is a reflector ring between the cathode and the gate with the inner diameter slightly smaller then the target volume. This ring is supposed to shield the events happening near the edge leaving only the evens in the middle, highly uniform, region of the TPC, to be detected.

2.2.2 Xurich II data processing

The raw data from the two PMTs in Xurich II are fed into a fan-in/fan-out module. One output is fed into a discriminator and then used as the trigger for the data acquisition. The other output is directly fed into the analog-to-digital converter (ADC) module. The raw data are saved in a ROOT format and needs to be processed first before any analysis can be done with it.

Originally Xurich II data were processed using the MATLAB software developed for the use in the original Xurich I detector. More details on that processor can be found in [33]. Later on the algorithm was translated into C++ and several improvements have been introduced over time.

The algorithm works as following. From the impedance of the electric circuit, the range and the resolution of the ADC the raw ADC counts are converted into a PMT output voltage. Using PMT calibration data the voltage is converted into photoelectrons. The baseline position and width are calculated from flat parts of the trace and subtracted from the signal. What is left should be either S1- or S2-like signals. Two different peak finders are then run, one searching for S1 signals, the other for S2. Once the S1 and S2 signals are identified, information about the position, height, width and several other shape parameters for the signals are calculated and saved into a ROOT tree. The information from the processed data can

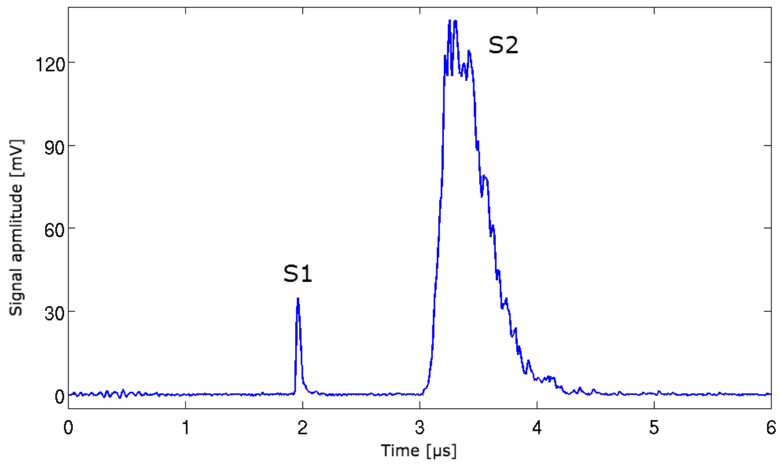

Figure 2.2.3: A typical waveform taken with the Xurich II detector using a ^{57}Co source. The prompt S1 signal is very fast and comparably small. The much wider S2 signal has a significant delay. The short drift time between the S1 and the S2 means that the event happened two millimeters below the gate. From the width of the S2 one can estimate that the gas gap is about 2 mm.

then be used to perform different types of physics analysis.

2.2.3 Xurich II goals and timetable

The main goal of the Xurich II detector is to measure the scintillation and ionisation signals from the nuclear recoils using the neutron generator. Before this a lot of preliminary work has to be done though. One needs to make sure all detector components work as intended. The gas recirculation system, the level meters and the PMTs needs to be calibrated. The energy calibration need to be done by measuring the detector response to electronic recoils using radioactive gamma sources. The sensitivity and systematic uncertainties need to be calculated from the same electronic recoil data. Monte Carlo simulations of the neutron lab and of the TPC need to be performed in order to determine the optimal experimental setup and get the expected neutron energy distribution and rate. On top of that, processing and analysis software need to be developed in order to extract physical information from the raw data.

The first version of the Xurich II TPC was finished in the beginning of 2013. Five operational runs were done with the original design. During the first run a problem with the field shaping rings occurred where they opened due to thermal stress. The operation of the detector continued anyway. After a failure of the signal connection, the detector was opened in an attempt to resolve the issue. After fixing the problem, the detector was closed and cooled down starting run 2. Run 2 was aborted after a similar connector failure. During the third run a problem with a feedthrough occurred, also a white powdery contamination was discovered in the detector. After a chemical analysis it was discovered that it is a silica-based gel, most likely coming from the silicon grease used for sealing the vacuum components. An attempt of cleaning the flanges was done and similar incident was observed since. Runs 4 and 5 ended due to failures of the PMT signal cables, level meter cables and issues with the high voltage circuit.

Due to to repeated failures of the cables, connectors, the high voltage resistors, and the issues with the opening of the field shaping rings, after run 5 a major redesign of the TPC was performed. All the signal cables were replaced by coaxial PTFE cables, high voltage cables were replaced by PTFE cables too. The LEMO connectors used in the original design were replaced by the more robust SMA connectors. The entire field cage was replaced by a new design featuring modified CF40 gaskets as field shaping rings. The feedthroughs ware also rearranged, separating the PMT high voltage and signal cables. Another feedthrough featuring an optical fiber was added in order to allow PMT calibrations using an external light source. The high voltage resistors were all placed on a single PCB board fixed to the side of the TPC. These upgrades were all done in an attempt to increase the reliability and the robustness of the TPC.

After the upgrade the operation was continued in spring 2014. Since then a couple of issues occurred with come connectors and a feedthrough. However, they could be easily resolved and the detector functions much better since then. As of September 2014 several calibrations with ^{57}Co, ^{83m}Kr and^{137}Cs gamma sources have been performed, the actual neutron measurements are still pending though.

Chapter 3

Calibration of Xurich II components and detector commissioning

Some hardware work is done in the scope of this thesis. This chapter will present the calibration of the level meters used for leveling of the detector, performance tests of various Xurich II parts and the continuation of the resistivity measurements of conductive PTFE which were done in [32].

3.1 Liquid level measurements

In Xurich II there are four level meters that can be used to determine the liquid xenon level in the detector. The level meters are simple capacitors. Because the dielectric constant of xenon is different in the liquid and in the gas phase, the capacitance changes depending on the amount of liquid between the plates.

Level meters 1-3 are parallel plate capacitors, placed around the TPC between the gate and the anode (see figure 2.2.2). They can be used to precisely determine the liquid level and also to determine if the TPC is tilted, by looking at the difference between the levels. The level meter 4 is a long cylindrical capacitor running along the length of the weir. It can determine the liquid level inside the weir and is mainly used when filling xenon into the detector.

The capacitance of the four level meters is measured with a Universal Transducer Interface (UTI), and the level can be determined from there. The UTI is a small sensor-interfacing device that can be used to measure different properties of an electric circuit and feed them in real time to a computer. The backsides of all the capacitors are connected together as a common, which acts as a reference point for the measurements. The UTI does not provide absolute capacitance values, but only the relative values in arbitrary units. Thus a calibration is required in order to convert the readout values into a real liquid level. For this we assume that the capacitance increases linearly with the liquid level. This is correct for perfect capacitor plates and it is a good approximation for our purpose.

3.1.1 Level meter calibration

In order to calibrate the level meters, the data from the UTI is taken during the filling of the detector. For each level meter the measured values are plotted into a histogram. The level measurement over time and the histogrammed plots can be seen in figure 3.1.1. The average minimum and maximum levels are then calculated from the peaks in the histograms. A rough estimate of the precision of the measurements is made based on the width of the peaks. In some cases it is difficult to say if the width is affected by the uncertainty of the measurements or by a physical change of the levels. This is especially true for level meter 4, since it is much longer then the other three. Moreover, as can be seen in figure 2.2.2, it is located in the weir and hence can easily get influenced by xenon recirculation. The results are summarized in table 3.1. Since the distance between the capacitor plates is known, the absolute resolution can be calculated for level meters 1-3. For the level meter 4 it is not clear what is the absolute level difference between the maximum and the minimum, so only the relative resolution is calculated.

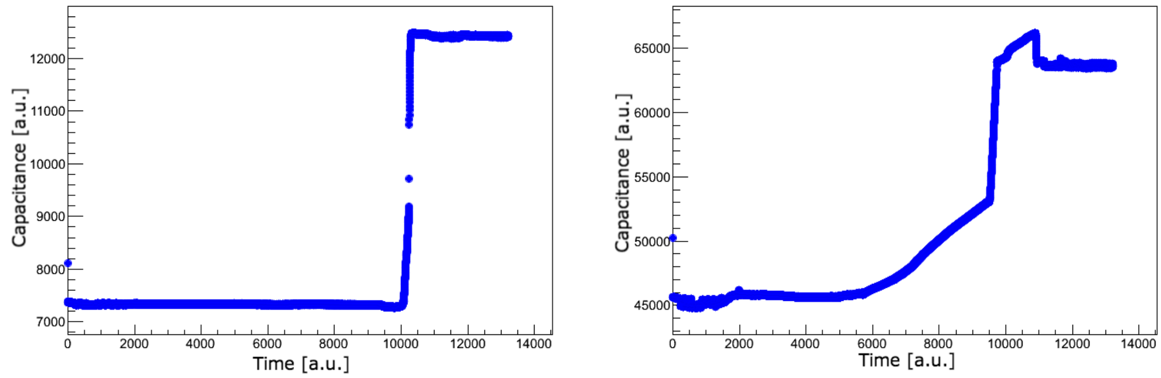

(a) The evolution of the capacitance over time. Level meters 1 and 4 are shown on the left and right respectively.

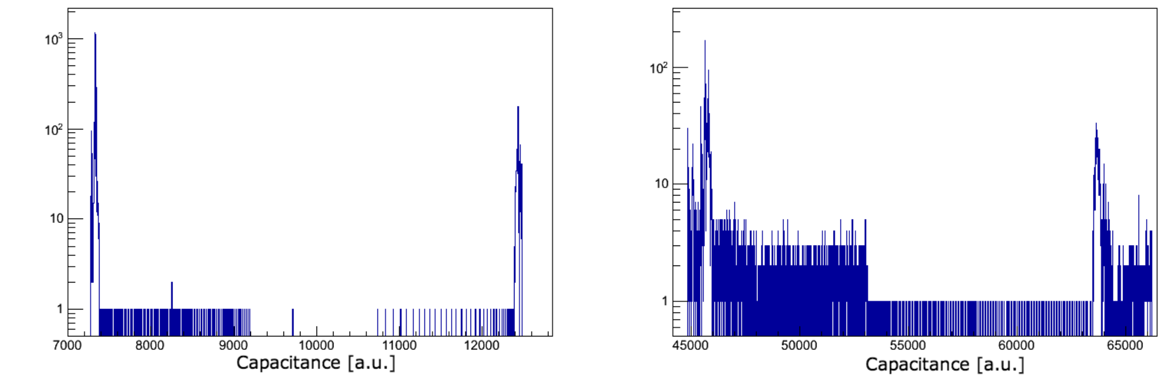

(b) The histogramed capacitances of the two level metes. From the peak positions one can determine the positions of the plateaus.

Figure 3.1.1: The measured capacitance for the level meters one the four in the Xurich II detector. The data for level meters 2 and 3 look very similar to the level meter 1, thus they are not shown here.

3.1.2 Liquid level determination through the measurement of the grid capacitance

After closing the cryostat in the preparation for run 6, we realized that the cable which is used as the reference point for all the four level meters when measuring the capacitance was short-circuited to the ground. Because of that, the readout of the level meter capacitance was not possible. In order to get a rough estimate of the liquid level we had the idea to measure the capacitance between the electrode grids.

A first attempt at measuring the capacitance between the grids, using the UTI, failed due to the limited range of the device. However, it turned out that an Arduino board [34] could measure the capacitance up to 10 nF and is suitable for the measurement of the capacitance between the grids.

It is worth pointing out that for these first tests only two simple wires were directly attached to the feedthrough that is usually used for the high voltage supply of the grids. The measurements presented here are mainly meant as a proof of concept, and if a decision is made to use this method in the future, a better cabling and connectors are needed. For this reason only the changes in the measured capacitance should be considered, since the absolute value tends to greatly change by moving the wires connected to the Arduino, or disconnecting and reconnecting them.

In order to investigate the effect of the liquid level on the measured capacitance, a two-step measurement is performed. First, the capacitance between the cathode and the gate is measured while xenon is being filled into the chamber. As expected, an increase of the capacitance with rising liquid level is observed. Once enough xenon is filled into the chamber to cover the grids, the Arduino is connected to

LM #	min level	max level	resolution
1	7326 (30)	12440 (50)	46 μm
2	9318 (30)	14569 (20)	27 μm
3	14298 (60)	19560 (30)	51 μm
4	45625 (500)	63650 (500)	4%

Table 3.1: The minimal and maximal capacitance values of the four level meters measured with the UTI, and the precision of the liquid level determination.

the anode and the gate, and a gradual recuperation is started. This leads to a decreasing liquid level, and as expected to a decreasing capacitance. The results of the two measurements can be seen in figure 3.1.2.

From the position of the plateaus at the start and at the end of the measurements one can determine the conversion rate between the capacitance and the physical liquid level, and from the width of the baselines estimate of the spatial resolution. The resulting values are given in table 4.3.

3.2 High-voltage circuit and field cage

For the upgrade of the Xurich II TPC it was decided to replace several electric components that proved to cause problems in the past. Namely all the cables and connectors as well as the high voltage circuit board were replaced. Before the introduction of the new components it had to be verified that they can sustain sufficient vacuum and the desired voltages.

3.2.1 Cables and connectors

For the PMT high voltage a commercial SMA connector is used. These are rated up to 500 V, however for our purposes we need them to operate at voltages of $800 - 950$ V which is the operating voltage for our PMTs. For this a simple test is performed, where two coaxial cables are soldered to the male and female parts of the connector. The cables are then individually put at a high voltage of 1000 V. The male and female parts are then connected together and again put at the same potential. In all three tests the connectors are left with the high voltage for ~ 10 min and no discharges, sparks, unexpected currents or damage on the connectors are observed. The conclusion is that the connectors can indeed be used for the high voltage supply of the PMTs.

For the high voltage of the cathode and the anode relatively thin PTFE coated wires are used. The question here was whether the thin PTFE coating can endure the voltages up to 9 kV that the cathode is designed for. For this test a ~ 30 cm piece of the PTFE coated wire is wrapped in aluminum foil. The foil is grounded and the wire is put at high voltage of up to 12 kV. No sparking or unexpected currents are observed, so the wires are deemed suitable for our high voltage applications.

The resistor board used to provide high voltage to the field shaping rings was originally made out of copper-plated PTFE. This design lead to several issues, where the board would deform under thermal stress. The soldering of the resistors to the board was a pretty challenging task as well. PCB, which is conventionally used as a base material for many electronic boards, would allow for a much cleaner design. It is however a known issue that some types of PCB tend to outgas a lot, which makes it impossible to reach sufficient vacuum. The outgassing might also severely compromise the xenon purity. A simple test was performed in order to check how much impact the implementation of such a board would have on our detector.

A short vacuum pipe with meshed gaskets on both sides is used as a chamber. The meshes on the gaskets prevent the samples from falling through. A vacuum pump is connected on one side of the pipe, and a gauge is connected on the other. A sample is placed into the pipe and the pump is turned on. The vacuum pressure we are aiming for is 10^{-6} mbar, since this is roughly the value required when pumping the detector chamber. As a first test, an empty ~ 2 cm $\times$ 2 cm PCB board is used. After a couple of hours of pumping we were unable to reach pressure below 10^{-4} mbar. Subsequently, a similar PCB board without a protective paint layer is tested and the desired vacuum of 10^{-6}mbar is reached. Since the

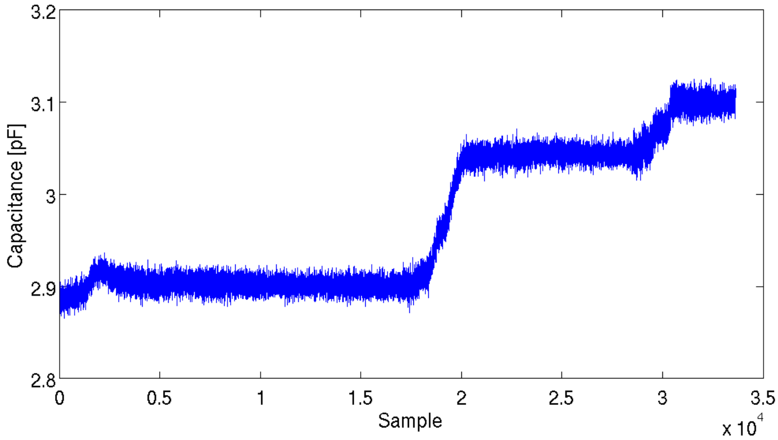

(a) Cathode capacitance measured over time. The two rises are due to filling of additional xenon.

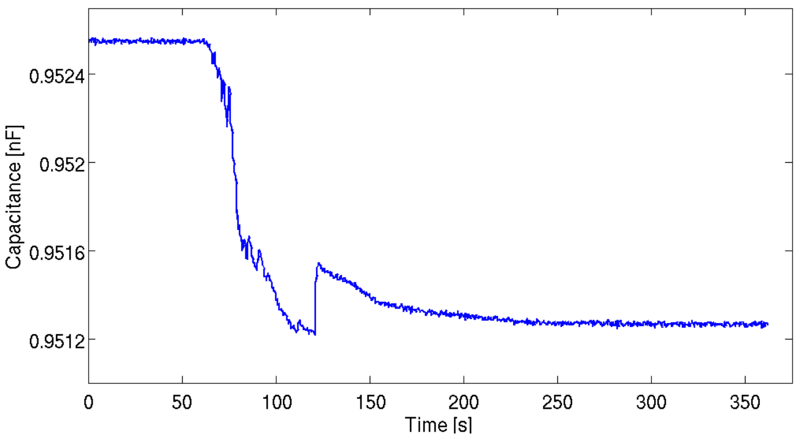

(b) Anode capacitance measured over time. The level was being lowered continuously. The jump around 120s is probably an artifact caused by bad electrical connection.

Figure 3.1.2: Calibration of the liquid level through measurements of the electrode capacitance

coating is mainly used to protect the board from dust and moisture, it is not necessary when operating the detector, so it was decided to use an uncoated PCB board for the high voltage circuit.

Using the same setup that was used for the PCB outgassing test, all the new cables and connectors are tested as well. Most of these components were used in vacuum before, so it is not expected to see any considerable amount of outgassing from them. Indeed, in all of the tests no impact on the vacuum quality could be observed.

3.2.2 High-voltage feedthroughs

The feedthroughs used to supply the high voltage to the anode and the cathode are the same as the ones used in Xurich I [35, 30]. The voltages used in Xurich II are higher then the ones used in Xurich I, so it needs to be verified that the feedthroughs can withstand them. For this a simple test is performed, where a high voltage is applied to the feedthrough.

The cathode feedthrough is put to voltages up to 10 kV, and no problems are observed. Since the cathode is designed to operate up to 9 kV it is decided that the cathode feedthrough does not require any further modifications. The anode feedthrough is put to voltages up to 4 kV. Above roughly 3 kV discharges inside the feedthrough are observed. Since the anode should be operated at 4 kV, it is clear that the feedthrough can not be used as it is and some additional insulation is required.

A hollow PTFE cylinder is made using a lathe. The cylinder can be put around the high-voltage part of the feedthrough and acts as an additional insulator. With this modification, the feedthrough can be put up to 5 kV without any issues.

3.3 Resistivity measurement of conductive PTFE at LXe temperature

As described in [32], properties of conductive PTFE have been measured before. In these tests no conductivity could be measured below ~ 240 K. In the final design of Xurich II, the cylindrical separator between the gate and the anode is nevertheless made out of conductive PTFE. The main reason behind this decision is that even at the operating temperature of around 180 K the conductive PTFE might still show some very low, but non-zero conductivity. Under normal operation in a detector built out of pure PTFE the drifting charges could over time build up on the PTFE walls. These charges would then have a negative impact on the electric field quality in that region. The remaining conductivity of the conductive PTFE might instead allow these charges to slowly dissipate. In order to quantify this effect, a much more precise measurement is done at $T = 180$ K in an attempt to determine the conductivity of conductive PTFE at these temperatures.

For the experiment a thin cylindrical plate of conductive PTFE is cut. The dimensions of the plate are $\varnothing = 63.5$ mm, $d = 3$ mm. A copper plate of similar dimensions is added on each sides of the PTFE cylinder to act as an electrode. The resulting "sandwich" is insulated with two bigger plates made out of normal PTFE in order to prevent the electrodes from touching anything. A positive high voltage is applied to the anode while the cathode is connected to a picoampere meter and then to the ground. A schematic drawing of the circuit can be seen in figure 3.3.1. A PT100 sensor is attached to the plates and a 4 point measurement of the temperature is performed with it.

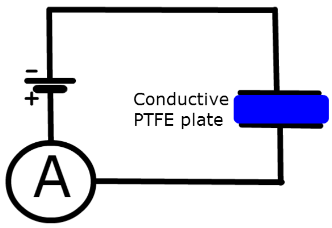

Figure 3.3.1: The circuit used to measure the conductivity of the PTFE. The PTFE plate is sandwiched between two copper plates, which are connected to a high voltage unit and ampere meter.

In previous measurements [32] we encountered the problem of water vapor from the air depositing on PTFE and leading to an increased current measurement. In order to reduce this problem, the measured plates are put into a plastic bag and thoroughly flushed with nitrogen gas. The bag is overpressurized and closed in order to prevent air from coming in. An attempt was also made to continue flushing nitrogen while doing the measurements. However this idea was abandoned because the continuous flow of warm nitrogen gas made it much more difficult to stabilize the temperature.

In order to cool down the sample, some liquid nitrogen is filled into a can. The sample is then slowly lowered down into the open nitrogen bath without dropping it into the liquid. With this process the sample can be cooled down to the desired temperature with the boil-off gas. The exact temperature can be controlled by changing the height of the sample above the liquid level. This method is obviously not very precise, the sample can be cooled down and stabilized within a couple of degrees from 180 K.

Once the sample is cooled down, a voltage of 2 kV is applied to one of the copper plates. Increasing the voltage would increase the precision of the measurement, however it would also lead to a considerable danger of creating discharges between the electrode plates and damaging our electronics. This is why

2 kV is used as a compromise. Using the picoampere meter a current of 2.0(5) nA is measured. The error is estimated from observing the fluctuations of the current over the course of a couple of minutes.

As a control, exactly the same measurement is done with the conductive PTFE being replaced with a normal PTFE plate of the same dimensions. The measured current is 2.0(5) nA, the same as with the conductive PTFE. Since it is known that normal PTFE is non-conductive, the measured current must originate from surface contaminations, bad calibration of the ampere meter or micro-discharges between the anode and the cathode. The precision of the measured current still allows to place a lower limit on the resistivity of the conductive PTFE:

$$I < \sqrt{2} \cdot 0.5\,\mathrm{nA} \approx 0.7\,\mathrm{nA}\,,$$

$$R > \frac{2\,\mathrm{kV}}{0.7\,\mathrm{nA}} = 2.8 \cdot 10^{12}\Omega\,,$$

$$\rho > 2.8\,10^{12}\Omega\frac{A}{l} = 3 \cdot 10^{12}\Omega\mathrm{m}\,.$$

This very high value is e.g. comparable to the conductivity of quartz glass [36]. Thus we do not expect it to have any influence on the electrical properties of our detector once it is cooled down to $\sim 180\,\mathrm{K}$.

Chapter 4

Simulations and data analysis

This part of the work is divided into three sections. They will explain the simulations of the neutron measurements, the various simulations of the electric field in Xurich II and an upgrade of the existing data processing algorithm by using a new χ^2-based approach.

4.1 Monte Carlo simulations of the neutron interactions with GEANT4

This section will explore the structure of the neutron beam and present the simulations performed in order to optimize the configuration for the neutron measurements.

4.1.1 Characterization of the neutron beam

The spectrum of the neutrons coming out of the generator was simulated before [27, 28]. For the simulations presented in 4.1.2 these previous results are used directly. However, after taking a closer look at the neutron spectrum some unexpected features became apparent. The previous simulations [27] do not offer an explanation for the structures, thus some further investigations about their origin are done. The fusion reaction in the generator creates isotropic monochromatic 2.45 Mev neutrons. Due to elastic scattering off atoms in the materials of the generator, one would expect the spectrum to have an exponential tail. This structure can indeed be observed in the neutron spectrum. On top of that there are several additional structures at lower energies. The two most prominent peaks are at roughly 1.6 MeV and 0.7 MeV. Both of these peaks show similar shape as the main 2.45 MeV peak with their exponential tail to lower energies. In addition to these, there are also several minor accumulations, for example around 1.8 MeV and 0.2 MeV. Because of the relatively low statistics of the simulation these smaller peaks are hard to pinpoint exactly.

The first idea to explain these structures is that due to the generator geometry there is some special preferred angle for elastic scattering which creates these secondary peaks. However, due to the similar shape of these secondary peaks, the sharp right edges, especially of the 1.6 MeV peak, and their relatively low energies, it seems very unlikely that these structures arise from simple elastic scattering. Thus an inelastic interaction with a nucleus is expected to occur somewhere in the generator material. So we are looking for a process of the type:

$$X + n \to X^* + n \to X + n + \gamma$$

In this process the neutron loses a part of its kinetic energy and excites a nucleus into a higher state. The excited nucleus is not stable and eventually de-excites by emitting a photon. Since the nuclear states have well defined energies, the emitted photon spectrum should have a sharp line at that energy. The energy of the photon is also expected to be roughly equal to the loss of neutron's kinetic energy. The generator output files provided by the previous work [27] also contain the information on the photons coming out of the generator. If we look at the photon spectrum in figure 4.1.1 we indeed observe several sharp lines, the most distinct ones being at 847 keV and 570 keV.

Keeping these results in mind and going back to the neutron spectrum allows us a clear interpretation of the structures: the primary 2.45 MeV neutrons scatter inelastically and lose energy equal to 847 keV and produce the secondary peak at 1.6 MeV. These neutrons can then scatter again and lose the same amount of energy, leading to the third peak at 0.7 MeV. Any of these neutrons can also interact with a nucleus through the other, rarer interaction, depositing 570 keV of energy and thus producing the smaller 1.8 MeV and 0.2 MeV structures. In figure 4.1.2 one can see how these transitions produce the observed spectrum.

As a final test for the hypothesis described above it would be beneficial if the two most prominent nuclear reactions could indeed be identified. For this the NuDat database [37] is used. Indeed two transitions are found:

$$^{56}Fe\, 2^{+} \rightarrow {}^{56}Fe\, 0^{+} + 846.8\, \mathrm{keV}$$

$$^{207}Pb\, \frac{5}{2}^{-} \rightarrow {}^{207}Pb\, \frac{1}{2}^{-} + 569.7\, \mathrm{keV}$$

Looking at the materials used in the simulation, it is identified that iron mainly comes from the stainless steel vessel that encompasses the fusion chamber of the generator. Lead is present in the shielding that was used at the exit of the generator in order to block gamma rays. For more detailed discussion about the use of the lead shield see [27].

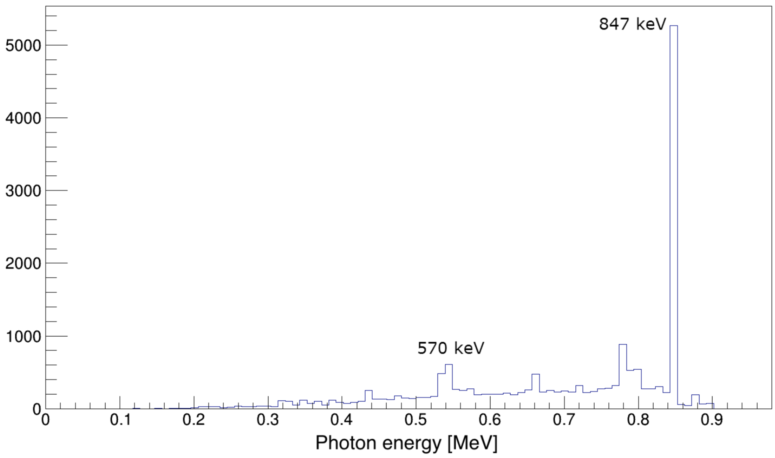

Figure 4.1.1: The energy spectrum of the photons coming out of the neutron generator.

4.1.2 Optimization of the TPC position

In order to be able to perform the neutron measurements with Xurich, a prior simulation is required to determine the optimal configuration of the experimental setup. The simulation is done in two steps. In the first part the neutron generator is simulated and the output is saved into a file. Subsequently, the second part is done using the results of the first step as the input and simulating the response of our detector to the generated neutrons. The first part of the simulation was done within [27], and the results are used here directly.

For the simulation the TPC is placed at a certain distance from the generator. Two scintillators are placed at a 45° angle from the neutron beam behind the TPC. Two identical scintillators are used at opposite sides in order to increase the event rate and reduce the systematic uncertainties. The neutrons coming from the generator scatter in the TPC and then get detected by the scintillator. Because of the fixed geometry, the energy the neutrons deposit in the detector can be directly calculated. The formula for elastic scattering is:

$$E_r = \frac{2E_n}{(1+A)^2}\left(1 + A - cos^2\theta - cos\theta\sqrt{A^2 + cos^2\theta - 1}\right)$$

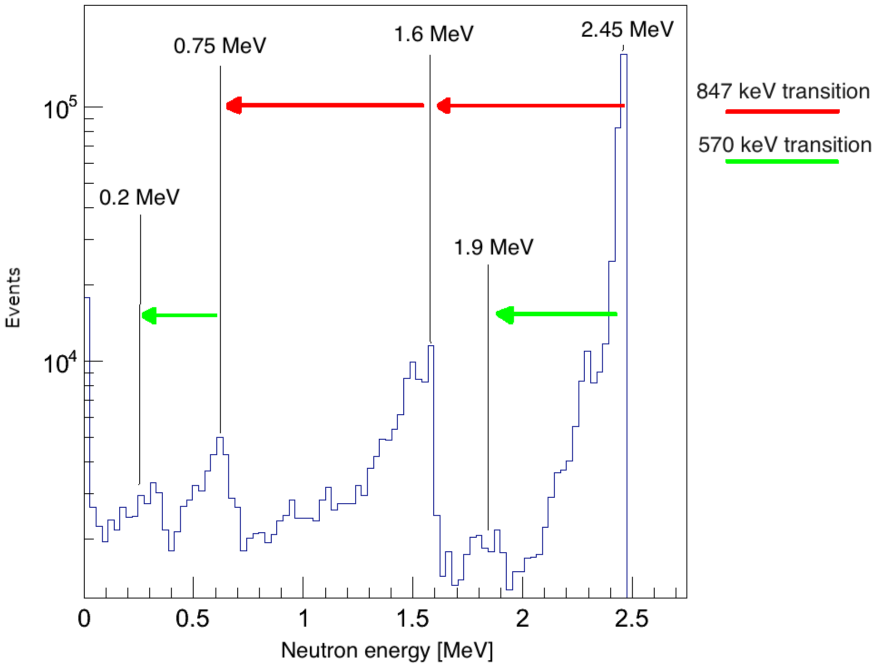

Figure 4.1.2: The neutron spectrum with the two nuclear transitions.

For 2.45 MeV neutrons and a scattering off a xenon nucleus (the average atomic mass of A=131 is used for the calculations here) at an angle of 45° we expect to see a peak in recoil energy at $E_r = 10.7\text{keV}$. The exact position and width of the recoil peak depends on the geometry of the setup. Thus several simulations are done for different distances between the generator and the TPC. Subsequently, the recoil spectra are compared for different setups with different TPC positions. These can be seen in figure 4.1.3.

As one can see, the spectra look qualitatively very similar. The rate is decreasing with increasing distance between the generator and the TPC. For the main recoil peak the position and the width are calculated, as well as the detection efficiency (the count of measured neutrons over the number of neutrons exiting the generator facility). The results for the three setups, as well as two other distances can be seen in figure 4.1.4. No substantial differences in the peak position and resolution can be observed, while a significant decrease in the efficiency is present. Thus the optimal solution would be to place the TPC as close to the generator as possible. In practice, this would be close to or slightly above the $d = 31$ cm value.

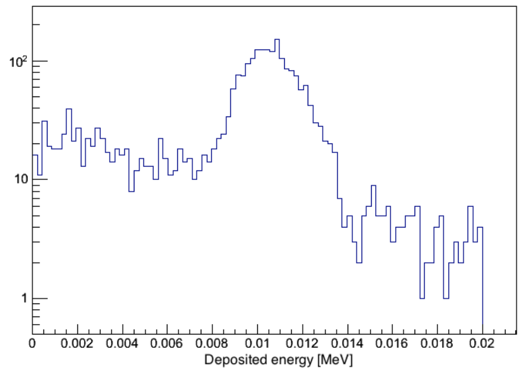

(a) $d = 231\ cm$

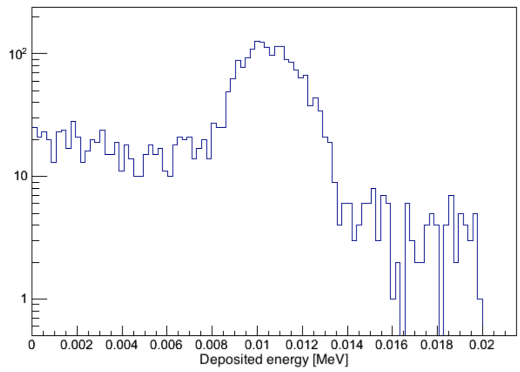

(b) $d = 131\ cm$

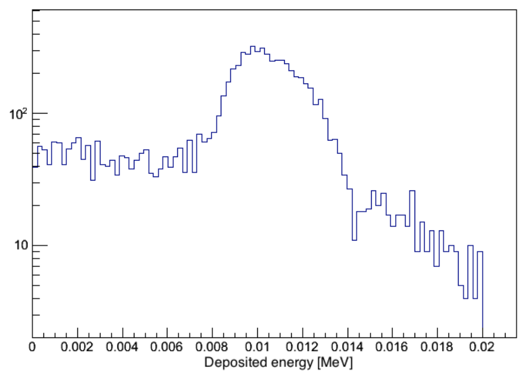

(c) $d = 31\ cm$

Figure 4.1.3: The spectrum of the energy deposited inside the TPC for different distance d between the generator and the TPC.

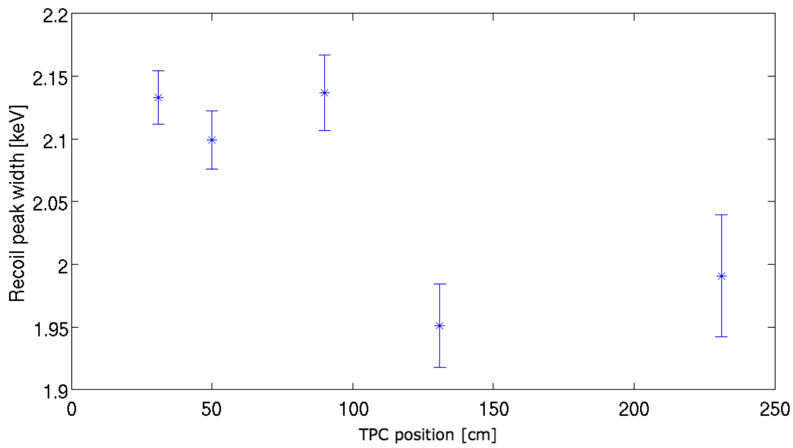

(a) Peak width for different TPC positions

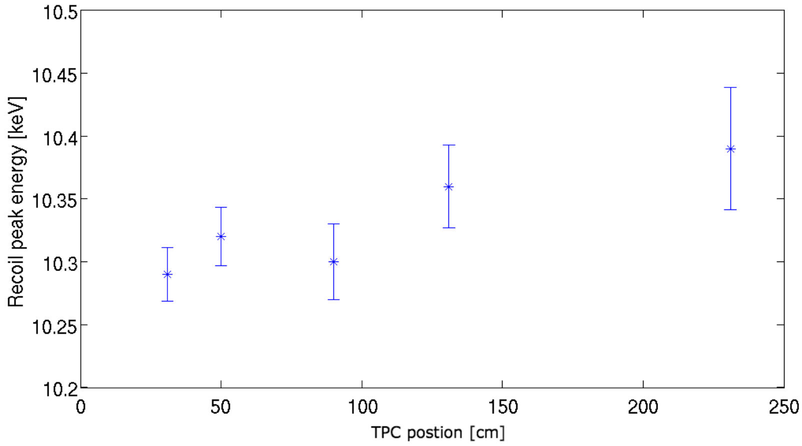

(b) Peak position for different TPC positions

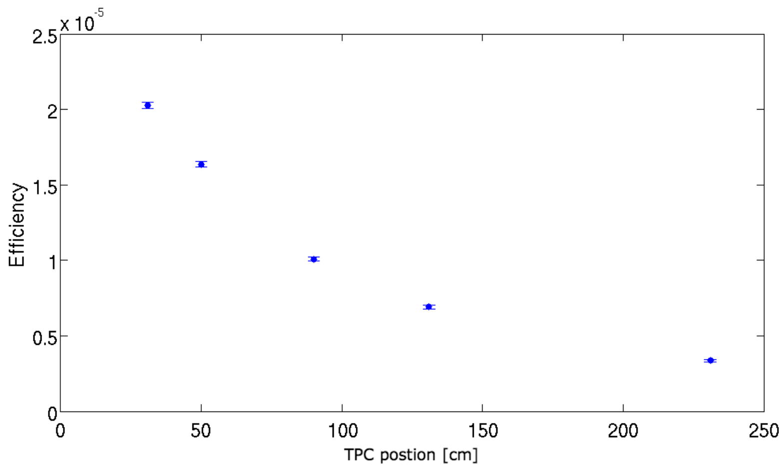

(c) Efficiency for different TPC positions

Figure 4.1.4: Efficiency and recoil peak characteristics for different TPC positions.

4.2 Electrostatic field simulations with COMSOL

Previously, in section 2.2.1, we established the need for a homogenous electric field. The original field shaping design for Xurich II was developed in [32]. Since then a couple of modifications to the TPC were performed and thus new simulations were required, which are presented in this section.

4.2.1 Optimization of the field cage and electric field uniformity

The layout of the Xurich II high voltage circuit has been discussed in [32]. For the upgrade of the field cage the basic design stays the same, however the dimensions and positions of the field shaping rings are slightly different in the new design.

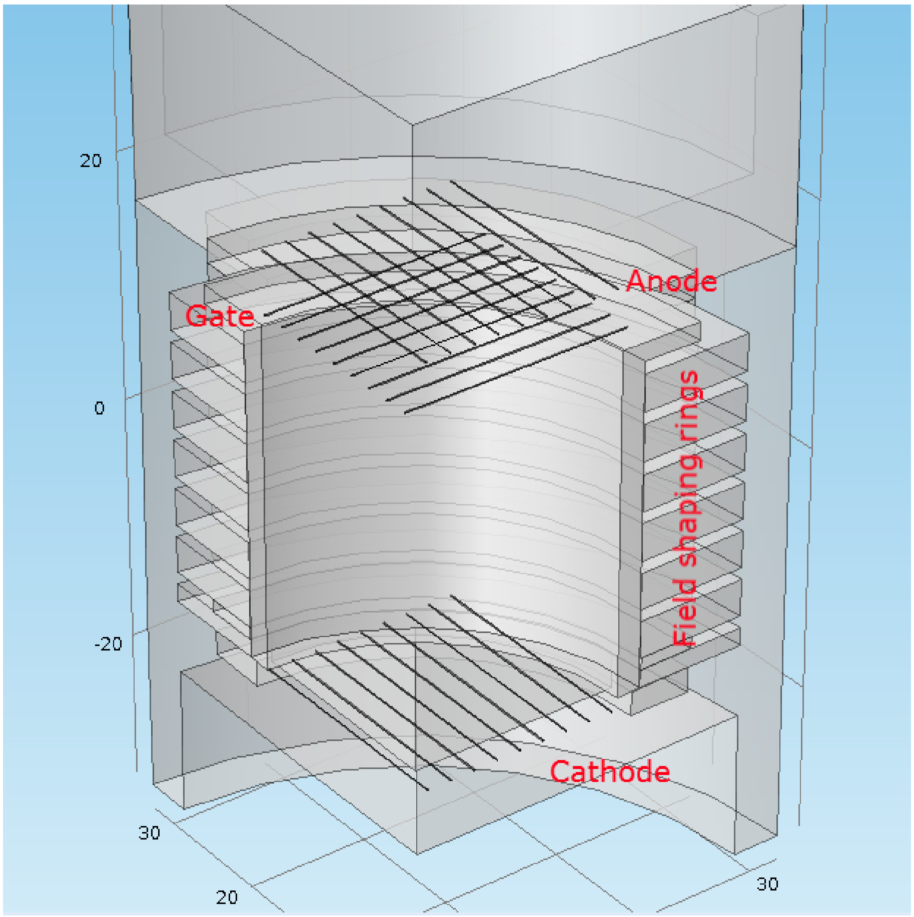

Figure 4.2.1: The model of Xurich II TPC used for the field simulations with COMSOL.

The model, shown is figure 4.2.1, is based on the model used for the previous field simulations [32] with some minor adjustments to the geometry. The voltage on the anode is set to $V_a = +4\,\mathrm{kV}$. The voltage on the cathode is varied between $V_c = -1\,\mathrm{kV}$and $V_c = -9\,\mathrm{kV}$. For each cathode voltage, the voltages on the top (V_1) and bottom (V_7) field shaping rings are adjusted manually such that the mean relative field deviation is as low as possible. The voltages on the other rings drop linearly with the ring number. This deviation is defined as:

$$r_E := \frac{\sqrt{\int (E - \bar{E})^2}}{\bar{E}}$$

The integral runs over the region of interest. In our case this is a cylinder in the active volume, excluding the regions within 1 mm close to the cathode, the gate, and to the PTFE reflector (see figure 2.2.2). The motivation behind these cuts is that the events near the edge of the TPC are not seen due to the PTFE shield between the gate and the anode. The field in the vicinity of the grids is highly distorted and not indicative to the overall quality of the field, so it is ignored. $\bar{E}$ denotes the electric field averaged over the same region of interest.

The optimal ring voltages are summarized in table 4.1.

V_c [V]	V_0 [V]	V_6 [V]
-1000	124	-830
-2000	18	-1660
-3000	-87	-2490
-5000	-296	-4150
-9000	-714	-7470

Table 4.1: Optimal voltages for the top (V_0) and bottom (V_6) field shaping rings for different cathode voltages.

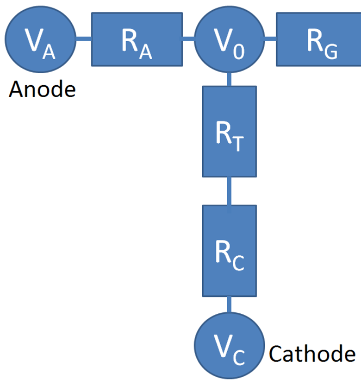

Figure 4.2.2: Schematic of the Xurich II high voltage circuit.
V_A, V_G, V_C represent the electric potentials for the anode, gate and cathode. V_0 is the voltage on the first (top) field shaping ring. R_A, R_G, R_C are the corresponding resistors. R_T represents the total resistance of the ring chain. Xurich II has seven field shaping rings, hence $R_T = 6R$.

If R denotes the value of the identical resistors between two adjacent field shaping rings, and for the cathode, the anode and the gate resistors we use $R_c = 1.4 \cdot R$, $R_a = 13.72 \cdot R$, $R_g = 0.926 \cdot R$, we can achieve the optimal voltages on the rings for any value of V_c. The circuit layout can be seen in figure 4.2.2.

After determining the optimal resistor values, a more precise simulation is run with the optimized setup in order to determine the mean relative field deviation as a function of cathode voltage. The results can be seen in figures 4.2.3, 4.2.4, 4.2.5, 4.2.6. These results are comparable to the results obtained in previous simulations [32], with the mean relative field deviations below 4.5% for cathode voltages above 2 kV. The final design of the high voltage circuit board can be seen in figure 4.2.7.

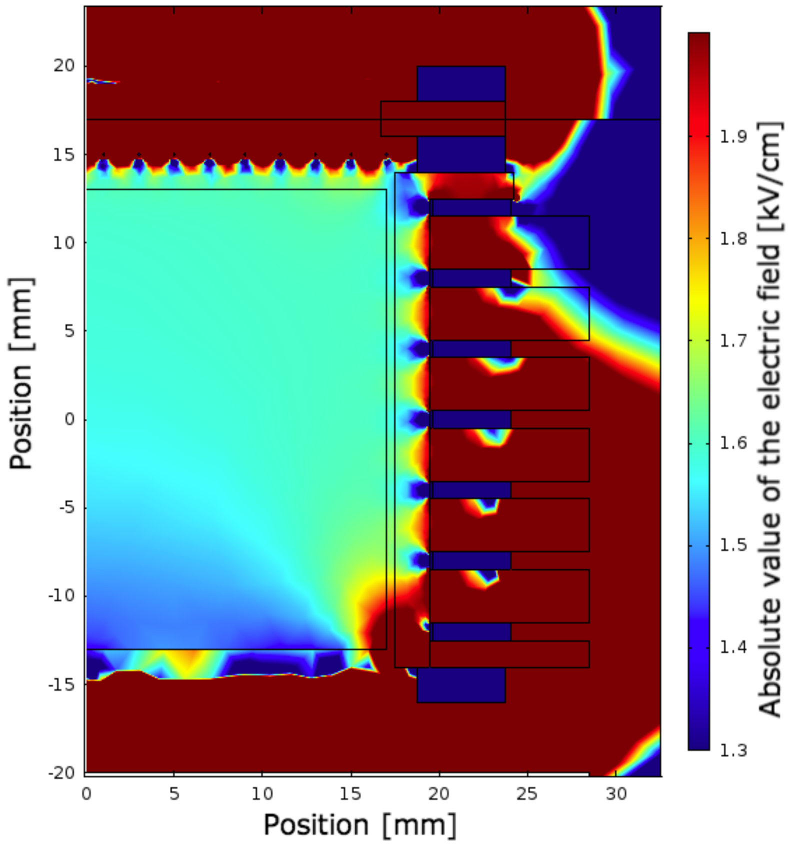

Figure 4.2.3: Cross section of the TPC with the absolute value of the electric field shown as color gradient. The anode is set to $4\,kV$, the cathode to $-5\,kV$. Simulation and the plot are done in COMSOL.

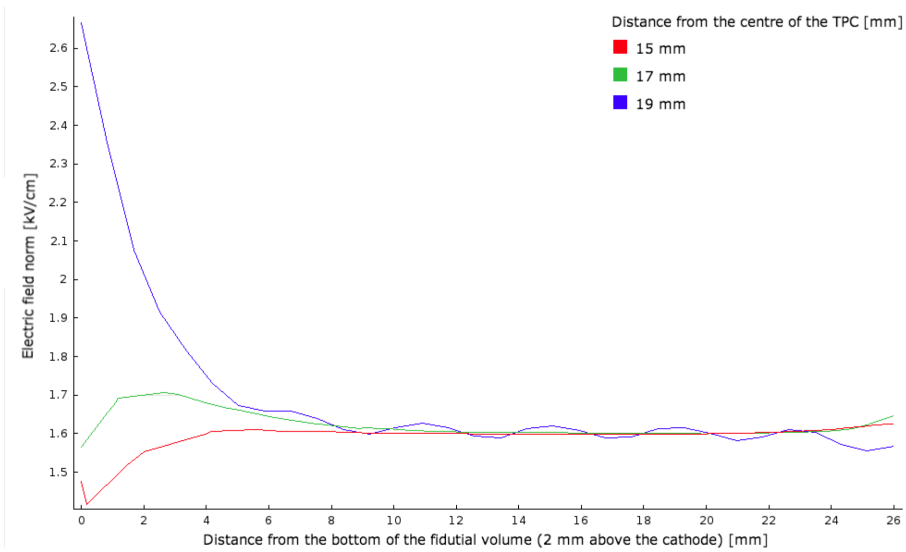

Figure 4.2.4: Electric field strength along vertical lines at different radii. The anode voltage is $4\,kV$, the cathode voltage is $-5\,kV$. The field 5 mm and more above the cathode is rather uniform. The non-uniformities near the cathode come mainly from the edges of the cathode ring.

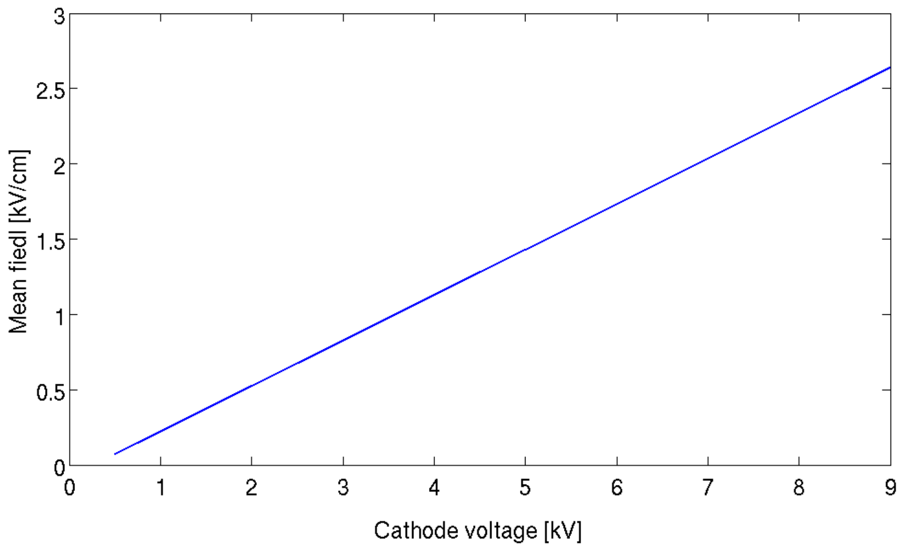

Figure 4.2.5: Mean electric field inside the TPC shown as a function of the voltage applied to the cathode. As expected, the behavior here is almost perfectly linear, with an offset due to field leakage. For more discussion of this effect see [32].

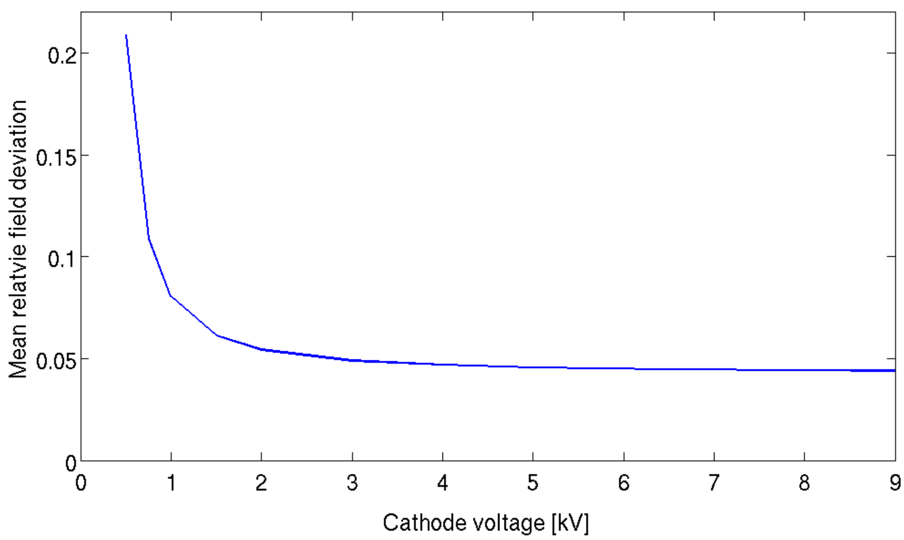

Figure 4.2.6: The mean relative field deviation inside the TPC, shown as a function of the cathode voltage. At very low cathode voltages the field is rather non-uniform. Most of these effects vanish above roughly 2 kV, and the residual mean field deviation is 4.4%.

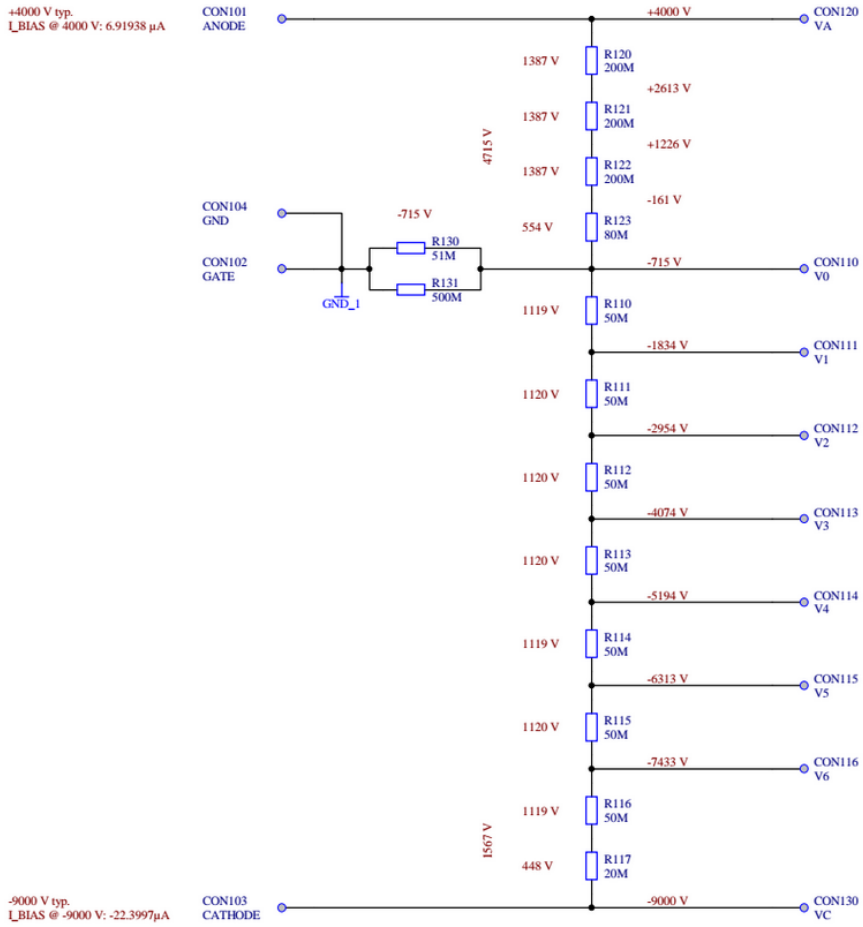

Figure 4.2.7: The final design of the high voltage circuit board.

4.2.2 Simulation of the alternative hexagonal grid design

An alternative to the wire grid design used in Xurich II would be hexagonally etched meshes. This design might lead to a more homogeneous field close to the electrodes, and might reduce some non-uniformities produced by the wire geometry. The replacement is not being actively planned yet, however a simple simulation of the design is done for Xurich II.

The main question to be answered with this simulation is whether a redesign of the high voltage circuit is required. In the Xurich II model discussed in the previous chapter the straight wire grids are replaced by hexagonal meshes. The pitch (the distance between two adjacent parallel wires) is left as a free parameter. For the reasons of simplicity the cathode voltage is kept fixed at $V_c = -4\,\mathrm{kV}$. For a pitch of $d = 2.5\,\mathrm{mm}$ the overall field in the region of interest is practically unchanged from the setup using wire grids. For comparison, the distance between the wires in design is $d = 2\,\mathrm{mm}$. If one wants to use a different pitch for the hexagonal meshes, a redesign of the high voltage circuit would be required.

It is also worth noting that the hexagonal grid might also have different optical properties from the wire grid. Practically the optical transparency might get compromised, thus leading to an overall lower light yield. To study this effect a completely different simulation needs to be done.

4.2.3 Simulation of the open field shaping rings

During 'baking' of the TPC (pumping at high temperature, ˜100°C, in order to induce outgassing of impurities from the surfaces of the detector components), the soldering of the field shaping rings opened creating small (~ 2 mm) gaps in the rings. The majority of the seven rings have been effected by the problem. A field simulation of the setup with open rings is done in order to determine how much the gaps effect the field inside the TPC. For the purpose of this simulation all gaps are alined on top of each other and all have the same size of 2 mm. The field strength inside the TPC is set to roughly 1 kV/cm. A comparison of the resulting field with and without the gaps can be seen in figure 4.2.8.

The relative average field deviation inside the sensitive region of the TPC is practically unaffected by the gaps (the mean relative field deviation goes up from 4.29% to 4.30%). Another two simulations are done for the lower (0.5 kV/cm) and the higher (2 kV/cm) fields in the TPC. No significant changes from the original configuration are observed.

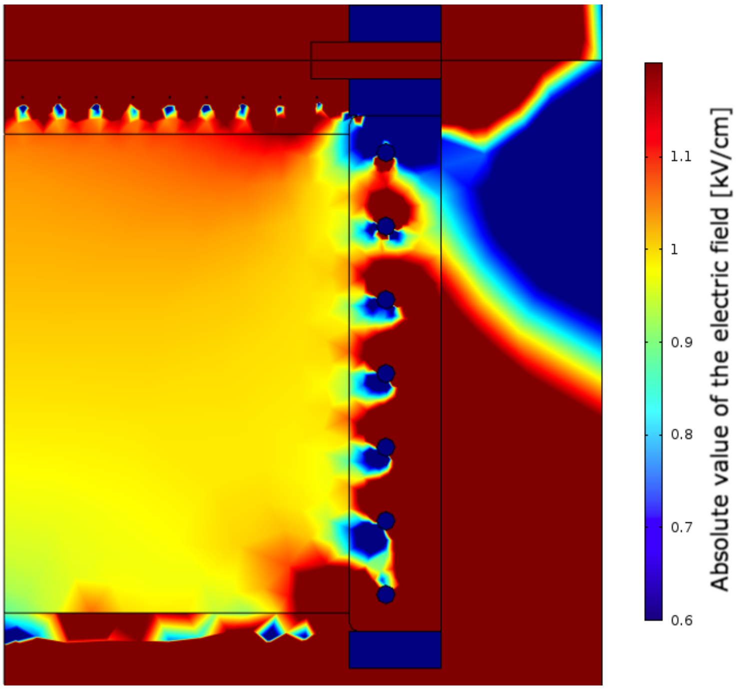

(a) Without gaps.

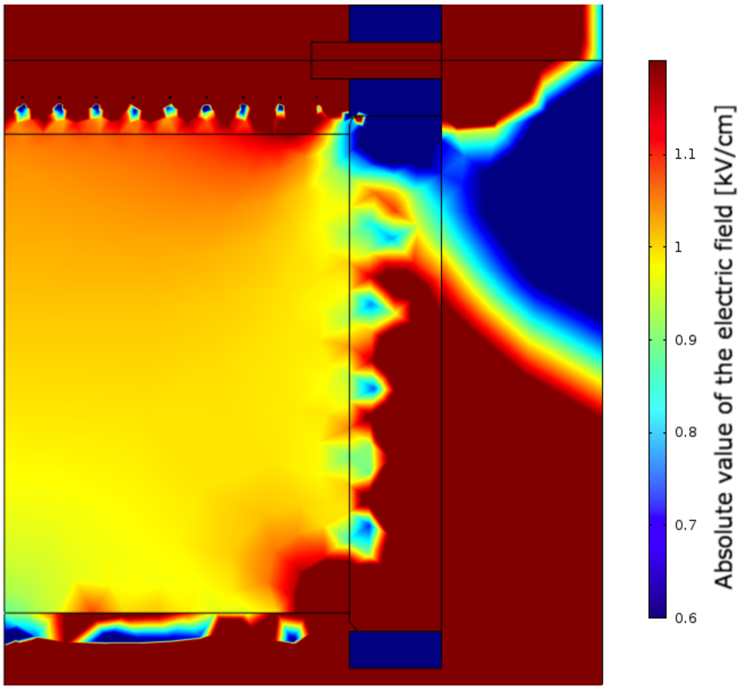

(b) With gaps.

Figure 4.2.8: Electric field inside the Xurich II TPC for a setup with closed field shaping rings and with rings where the 2 mm gaps are introduced. Minor changes can be seen directly next to the gap, but overall field is unaffected.

4.3 Data processing

The Xurich II data acquisition system was introduced in section 2.2.2. Using the original data processing algorithm, several problems were discovered. This lead to the development of a new processing algorithm.

This section will discuss the new algorithm and offer some comparison between the two.

The original peak finding algorithm described in [33] shows the following problems:

- very small S1 signals are often not recognized by the algorithm;
- S1 pulses that are close to subsequent S2 pulses are sometimes misidentified as a part of the S2 structure;
- S2 pulses with a high amplitude, but a small width are sometimes misidentified as S1 signals.

These problems are not terminal and the algorithm still can be used to obtain useful data, however it became obvious that there is some room for improvement.

Looking at the problems mentioned above it is clear that they can be eliminated by finding a better way of deciding if a structure is S1-like or not. Thus a new S1 finder algorithm is developed to identify all S1 structures in a trace. All the remaining signals above a pre-defined threshold can then be assumed to be S2-like.

4.3.1 χ^2 -based peak finder algorithm

The idea behind the algorithm is that the shape of all the S1s is fairly similar, since it mainly depends on the response time of the PMTs and not on the shape of the actual light pulses. Particularly the shape of S1 signal does not depend on its amplitude.

Thus the algorithm is divided in two parts. In a first step we need to find out what is the shape of a typical S1 signal. In a second step we can then compare a signal in a trace with this template. If the two look similar we tag the signal as an S1.

For the first part one needs a large sample of signals that are known to be S1s. In order to get this, one can simply take calibration data with zero field conditions. This ensures that almost all the signals are S1s and they can easily be identified with the default peak finding algorithm. The part of the trace containing the S1 is saved (empirically it turns out 200-300 ns long template is sufficient). These short S1 traces are normalized to have the same integral and aligned such that the maximum is in the same position. The median is then taken bin by bin. The median is used instead of the average since it makes the method more robust against outliers coming from noisy events or misidentified S1s. After renormalizing the median to have unit integral we get the desired S1 template.

For every signal trace we can then use this template to find the S1s. If t_i is template of length m and s_i is the investigated trace, then we define the χ^2 as following:

$$\chi_i^2 := \sum_{j=1}^{m} \left(\frac{s_{i+j}}{\sum_{k=1}^{m} s_{i+k}} - t_{i+j} \right)^2$$

If the trace contains an S1, the χ^2 at that point has a very low value, since the normalized S1 and the template are similar. There might be a constant offset, depending on the position of the maximum inside the template. This can easily be corrected by shifting the index of χ^2 by the same amount. If we have an S2-like structure, noise or just the baseline, the χ^2 value is rather large. In this way a threshold can be defined, and if the χ^2 value falls below that, we identify the S1 in the trace. The optimal value for the threshold can depend on the noise level of the measurement and on the type of analysis that one wants to perform.

4.3.2 Algorithm validation on the calibration data

A series of ^{57}Co and ^{83m}Kr data was taken during the 6th cooldown. While the ^{57}Co emits monochromatic photons, ^{83m}Kr decays via an intermediate ^{83m*}Kr state. This state has a very short lifetime, so two photons of 32.1 keV and 9.4 keV are emitted within a short time window. This property of ^{83m}Kr combined with relatively low photon energy allows for some interesting analysis. Another advantage is that krypton can be mixed with xenon and directly injected into the TPC allowing for a much more uniform event distribution than with external sources such as ^{57}Co. One of the first studies on liquid xenon chamber calibration with ^{83m}Kr has been performed with Xurich I [35].

Some basic analysis of the Kr data is done here, with the main focus on the comparison between the two S1 peak finder algorithms (the original method using the S1 filters and the χ^2-based algorithm)

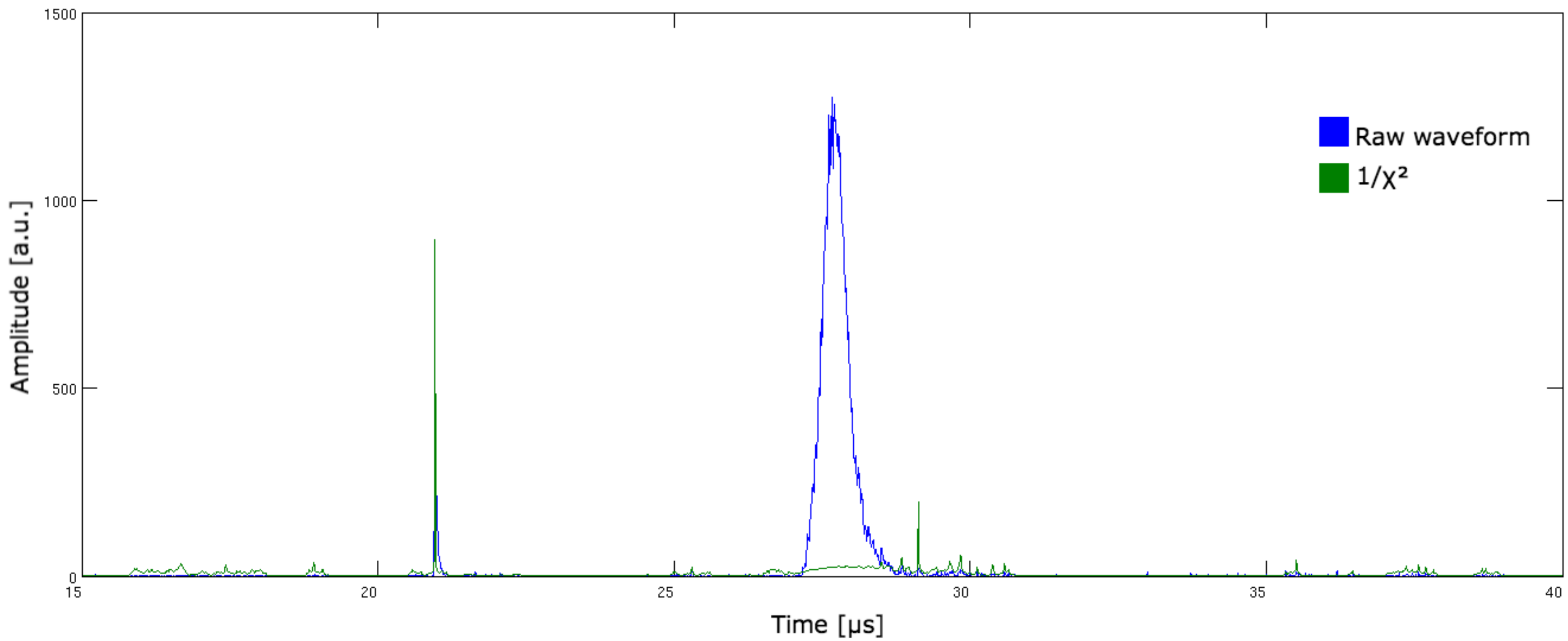

Figure 4.3.1: An example of the performance of the χ^2 S1 finder on a ^{57}Co trace. The trace is in blue, the corresponding χ^2 filter is in green (for better visibility the inverse of the χ^2 is actually plotted). Around 21 µm there is an S1 signal and the $1/\chi^2$ parameter indeed has a pronounced peak at this position. At ~ 28 µs there is an S2 signal and the χ^2 barely reacts. At ~ 29 µs there is a noise structure which produces a local minimum in the χ^2. By using appropriate cuts on the χ^2 values, one can distinguish these noise peaks from the actual signals.

and their ability of identifying the two S1 peaks of Kr. Some basic cuts are used for the entire analysis, namely the requirement that both PMTs see at least 2 S1 signals and the coincidence between the signals in the two PMTs (50 ns). First we take a look at the S1 spectrum resulting from the χ^2 processing. A sum of two Gaussian functions is fitted to the spectrum. The results can be seen in table 4.2 and figure 4.3.2.

E	32 keV	9.4 keV
PE	142	62.5
light yield [PE/keV]	4.4	6.6
resolution	24%	28%

Table 4.2: Results from the fit of the ^{83m}Kr data

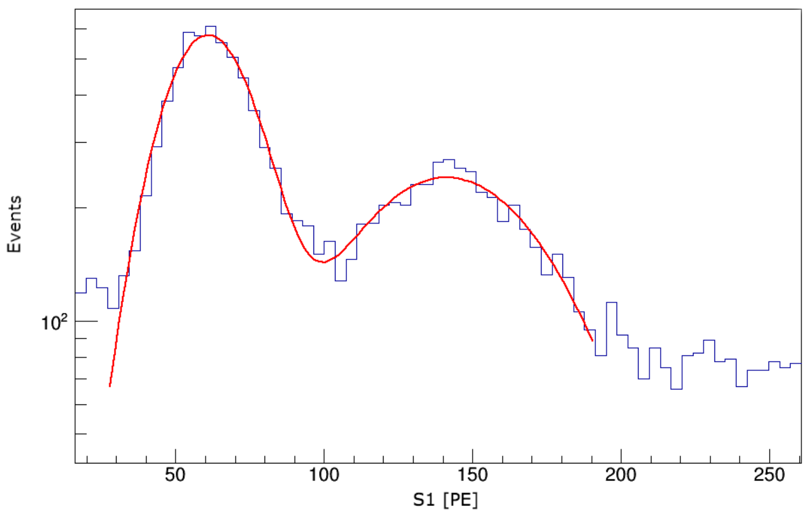

Figure 4.3.2: S1 area with the fit of the two ^{83m}Kr peaks. The fit parameters can be found in table 4.2.

From these values two additional sets of cuts are created visualized in figure ??:

- C1 is a cut on the energy of the first S1. It is a 3 σ cut around the main peak.
- C2 is a cut on the energy of the both S1s. It is an elliptical 3 σ cut around the main peak in the first S1 vs second S1 plane.

Three different data sets are analyzed using these cuts; a ^{83m}Kr data set processed with the χ^2 algorithm, the same data set processed with the filter-based S1 finder and a ^{57}Co data set processed with the old algorithm. The spectra can be seen in figure ??. The ^{57}Co data set should not contain any ^{83m}Kr events. Since the energy of the^{57}Co γ-rays is much higher, also no leak of the actual ^{57}Co events into the region of interest is expected. Thus we can assume that all the events in the region of interest are due to background. In the ^{83m}Kr data set the events within the C1, but outside of the C2 region can also be assumed to be background events or events where the second ^{83m}Kr peak was not properly identified. The events in the C2 region are either real ^{83m}Kr events or events due to the same background that appears in the other region. In order to get an estimate on our signal-to-background ratio in the C2 region, we do the following. The event counts of the three data sets are scaled in a way that the number of events in the C1 subtracting the C2 region are the same in all of them. After the rescaling, the number of events in the C2 region from the ^{57}Co data set is taken as the background, and the difference between the number of C2 events in ^{57}Co and ^{83m}Kr data sets is taken as the number of signal events. Our S/B is the ratio of the two numbers.

This procedure gives us a S/B of 0.07 for the old processing method and 20.5 for the χ^2 method. These results might be somewhat biased since we assumed that the background looks the same for both processing methods. This might not be true since a lot of this background could come from some misidentified events and thus depend on what processing method one uses. The discrepancy of the S/B values is however so large that it is very unlikely that a slight change in background could have a strong effect.

As the next step the lifetime of the intermediate ^{83m*}Kr state is computed. For this we only use data set processed with the χ^2 algorithm, because, as we have seen, the other processor does not provide us with any meaningful signal. For the events within the C2 region we look at the timing difference between the two S1 peaks and fit an exponential function to the the distribution. The fit can be seen in figure 4.3.4. From the slope we deduce a lifetime of $\tau = 225(5)$ ns, consistent with the previous measurements [35] and with the published value of $\tau = 218$ ns [37].

	Cathode-Gate	Anode-Gate
Difference in the capacitance	213 fF	1281 fF
Capacitance resolution	7 fF	7 fF
Capacitance-to-level conversion factor	188 um/fF	3 um/fF
Resolution of the level	1.3 mm	20 um

Table 4.3: Capacitance to position conversions calculated from the electrode capacitance data sets.

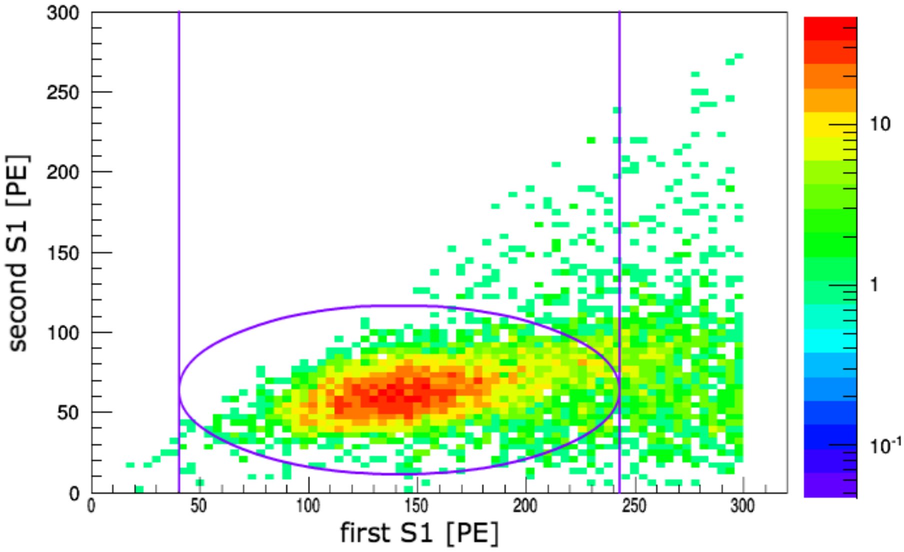

(a) Kr data set processed with the χ^2 peak finder algorithm.

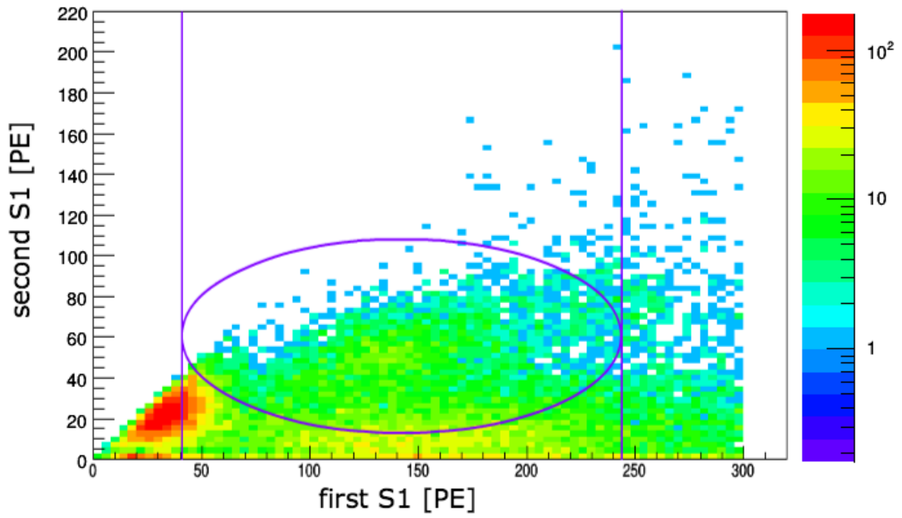

(b) Kr data set processed with the default peak finder algorithm.

Figure 4.3.3: The area of the first S1 versus the area of the second S1 in the ^{83m}Kr calibration data. The purple lines show the cuts described above. C1 is the cut between the two lines and C2 two is represented by the ellipse. The Co data set is not shown here, since the plot is qualititavely indistinguishable from the Kr data set processed with the filter-based algorithm.

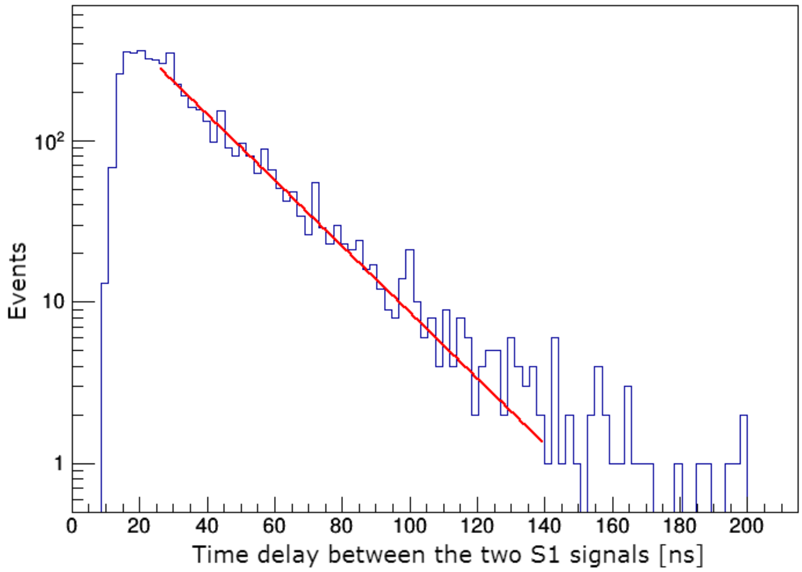

Figure 4.3.4: Delay time between the two S1 signals fitted with an exponential function. From the fitted slope ($4.44\ \mu s^{-1}$) one can calculate the lifetime of the ^{83m*}Kr state. This yields $\tau = 225(5)$ ns, consistent with the published value of $\tau = 218$ ns [37]. At short delay times there is a sharp fall off due to the inability of the algorithm to distinguish two signals if they are too close to each other.

Chapter 5

Conclusions

The Xurich II detector is an R&D project, designed for measurements of scintillation and ionization yields for low-energy nuclear recoils. The main hardware work done in the scope of this thesis can be separated in three parts. The first one focuses on the liquid level in Xurich II and includes the calibrations done with the level meters in order to achieve an accurate measurement of the liquid level. A new method using the electrodes to estimate the liquid level without using the level meters is developed. It does not seem as reliable or accurate as the level meters, however it can be useful in case of level meter failure. The second part includes the high voltage circuit for the electric field cageand the measurements performed on the various components of the circuit in order to ensure that they can endure both the high voltages and the vacuum level. The majority of the tested parts fulfill all of our requirements; for the ones that do not, slight modifications had to be performed. The last part is dedicated to the measurements of the resistivity of conductive PTFE at liquid xenon temperatures. This part closely connects to the measurements presented in my bachelor thesis [32]. At the end no conductivity could be measured at 180 K, however a new upper limit on the conductivity is set.

The software work also consists of three parts. The first one presents the neutron laboratory and the Monte Carlo simulations performed with GEANT4 in order to characterize the neutron beam spectrum and to optimize the exact experimental setup in the neutron laboratory. No considerable advantage of moving the TPC away from the generator is found, while moving the TPC closer to the generator increases the event rate. Because of that it seems to be advantageous to have the detector as close to the generator as possible. In practice this would be approximately 30 cm away from the generator opening.

Next part of the software work introduces the electrostatic field simulations for Xurich II. The simulations are done with COMSOL and the majority of them were already presented in [32]. However due to some modifications of the Xurich II geometry the simulations had to be modified and rerun. From the simulations the optimal configuration of the high voltage circuit is calculated. Additionally the possibility of a new hexagonal grid design is explored. From the simulations it seems that if one chooses a pitch of 2.5 mm, the current grids could be replaced by hexagonal ones without having to modify the high voltage circuit. Due to thermal expansion during heating of the detector chamber gaps in the field shaping rings were created. The impact of these gaps on the overall field is also simulated and no considerable negative impact is found.

An upgrade to the existing processor for the Xurich II data is developed. The main goal of the upgrade is to improve the S1 peak finder algorithm and improve the sensitivity to very small scintillation signals. The new algorithm is presented and its performance is compared to the old one by using both of them to process the same data sets and comparing the results. For the low energy ^{83m}Kr events a vast improvement is observed, with the old algorithm hardly detecting the events at that low energy of ~ 10 keV, and the new one showing a nice double peak as expected. The calculated lifetime of the intermediate ^{83m*}Kr state of 225 ns also agrees with the literature value of 218 ns.

Conclusively, even though no neutron measurements were performed with Xurich II and thus the goal of measuring the $\mathcal{L}_{eff}$ has not been reached yet, a lot of important studies have been performed and presented in this thesis, which should facilitate the future measurements done with the detector.

Bibliography

[1] K. G. Begeman, A. H. Broeils, and R. H. Sanders, Mon. Not. Roy. Astron. Soc. **249**, 523 (1991)

[2] T.S. van Albada *et al.*, Astrophys. J. **295** (1985) 305

[3] A.Dressler, Astrophys. J. **281** (1984) 512

[4] Kenneth Rines *et al.* Astrophys. J. **657** (2007) 183

[5] F. Zwicky, Helv. Phys. Acta **6**, 110 (1933)

[6] A.Diaferio, S.Schindler, K.Dolag *Clusters of Galaxies: Setting the Stage* Space Science Reviews **134** (2008) (1–4): 7–24

[7] NASA, N. Benitez (JHU), T. Broadhurst (Racah Institute of Physics/The Hebrew University), H. Ford (JHU), M. Clampin (STScI),G. Hartig (STScI), G. Illingworth (UCO/Lick Observatory), the ACS Science Team and ESA

[8] M. Markevitch, A. H. Gonzalez, D. Clowe, A. Vikhlinin, L. David, W. Forman, C. Jones, S. Murray, and W. Tucker . "Direct constraints on the dark matter self-interaction cross-section from the merging galaxy cluster 1E0657-56". Astrophys.J. **606** (2003)

[9] Douglas Clowe *et al.,* Astrophys. J. **648** (2006) L109

[10] Penzias,Wilson Astrophys. J. **142** (1965) 419–421

[11] Percival, W. J. *et al.*, "Baryon Acoustic Oscillations in the Sloan Digital Sky Survey Data Release 7 Galaxy Sample". Monthly Notices of the Royal Astronomical Society **401** (2010)

[12] ESA and the Planck Collaboration esa.int/spaceinimages/Images/2013/03/Planck_CMB

[13] Lars Bergström, New J. Phys. **11** (2009) 105006

[14] WMAP Collaboration, J. Dunkley et al., Astrophys. J. Suppl. **180**, 306 (2009)

[15] G. Jungman, M. Kamionkowski, and K. Griest, Phys. Rept. **267**, 195 (1996)

[16] Douglas Clowe *et al.* Astrophys. J. **648** (2006) L109

[17] Riccardo Catena and Piero Ullio JCAP **08** (2010) 004

[18] Charlotte Strege, Roberto Trotta, Gianfranco Bertone, Annika H. G. Peter, Pat Scott, Phys. Rev. D **86**, 023507 (2012)

[19] E. Aprile *et al.*, *The neutron background of the XENON100 dark matter experiment*, J.Phys. **G40** (2013) 115201

[20] E. Aprile *et al.*, Astropart.Phys. **35** (2012)

[21] LUX Collaboration, Nuclear Inst. and Methods in Physics Research **A704** (2013)

[22] E. Aprile *et al.*, *Conceptual design and simulation of a water Cherenkov muon veto for the XENON1T experiment* preprint: arXiv:1406.2374 (2014)

[23] J. D. Lewin and P. F. Smith, Astroparticle Physics **6**, 87 (1996)

[24] P. Sorensen *et al.*, Nucl. Instrum. Meth. **A601**, 339 (2009)

[25] E. Aprile *et al.*, Phys. Rev. **D72**, 072006 (2005)

[26] A. Hitachi, Astropart. Phys. **24**, 247 (2005)

[27] D. Biasini, *Monte Carlo Simulation of a Liquid Xenon Detector Response to Low-Energy Neutrons*, Bachelor Thesis, University of Zürich (2014)

[28] P. Pakarha, *Preparations for measurements of the low energy response of liquid xenon,* Master Thesis, University of Zürich (2012)

[29] E. Aprile *et al.*(XENON Collaboration), *Dark Matter Results from 100 Live Days of XENON100 Data* Physical Review Letters vol.107, Issue 13, id. 131302

[30] Laura Baudis, Hrvoje Dujmovic, Christopher Geis, Andreas James, Alexander Kish, Aaron Manalaysay, Teresa Marrodan Undagoitia, Marc Schumann , *Response of liquid xenon to Compton electrons down to 1.5 keV,* Phys. Rev. **D87** 115015 (2013)

[31] Aprile et al., IEEE Transactions on nuclear science, Vol. 51, No. 5, October 2004

[32] H. Dujmovic, *Simulation and Optimization of the Electric Field in a Liquid Xenon Time Projection Chamber*, Bachelor Thesis, University of Zurich (2012)

[33] A. Manalaysay, *Response of liquid xenon to low-energy ionizing radiation and its use in the XENON10 dark matter search*, Ph.D. Dissertation, University of Florida (2009)

[34] Documentation page, www.arduino.cc/en/Main/ArduinoBoardUno

[35] A. Manalaysay, T. Marrodan Undagoitia, A. Askin, L. Baudis, A. Behrens, A. Kish, O. Lebeda, D. Venos, *Spatially uniform calibration of a liquid xenon detector at low energies using 83m-Kr*, Review of Scientific Instruments **81**, 073303 (2010)

[36] Raymond A. Serway, *Principles of Physics*, Fort Worth, Texas (1998)

[37] Nuclear Structure and Decay Data website, www.nndc.bnl.gov/nudat2